A Markov chain Monte Carlo approach for geostatistically simulating mass-conserving subglacial topography

Niya SHAO,[1] Emma J MACKIE,[1] Michael J FIELD,[1] Felicity S MCCORMACK[2]

[1] *Department of Geological Sciences, University of Florida, Gainesville, FL, USA*

[2] *Securing Antarctica's Environmental Future, School of Earth, Atmosphere and Environment, Monash University, Clayton, Kulin Nations, Victoria, Australia.*

ABSTRACT.

Subglacial topography is critically important for simulating ice sheet evolution and projecting sea-level contributions. However, the subglacial topography of the Antarctic Ice Sheet is sparsely measured. Obtaining a gridded topography map used in ice sheet simulations requires interpolating the sparse measurements or inverting topography from observations of ice velocity and surface elevation. Traditional inverse methods based on the mass conservation law often produce a single topography that is overly smooth and does not capture the non-uniqueness of the solutions to mass conservation. Instead of solving for a single topography deterministically, stochastic methods can be developed to simulate equiprobable realizations of mass-conserving topography with realistic roughness. In this study, we develop a new algorithm that combines geostatistical simulations with Markov chain Monte Carlo (MCMC) to stochastically generate subglacial topography realizations for Denman Glacier. The final topography ensemble shows significant elevation differences to BedMachine and large topographic uncertainty. This topography ensemble can be incorporated in ensemble modeling, allowing the propagation of topographic uncertainty to the uncertainty in sea level contribution predictions.

INTRODUCTION

Subglacial topography, the bed elevation beneath the ice, plays a key role in the evolution of glaciers and ice sheets. In coastal regions, grounding line retreat is associated with the slope, curvature, and elevation of the subglacial bed (Weertman, 1974; Schoof, 2007; Bradwell and others, 2019; Sergienko and Wingham, 2022). Thus, variations in different topography realizations can directly affect the simulated ice-stream stability (Gasson and others, 2015; Wernecke and others, 2022; Castleman and others, 2022). Subglacial topography is also an essential component in modeling englacial and subglacial processes. For example, previous studies have demonstrated how subglacial topography influences basal traction (Bingham and others, 2017; Kyrke-Smith and others, 2018; Hoffman and others, 2022), geothermal heat flow (Colgan and others, 2021; Shackleton and others, 2023), ice deformation (Meyer and Creyts, 2017; Law and others, 2023), and subglacial hydrology (Siegert and others, 2016; MacKie and others, 2021b), each of which significantly impacts ice sheet evolution, and hence the projected sea level rise contributions.

Despite its importance, subglacial topography under the Antarctic Ice Sheet is only sparsely measured. Bed elevation measurements are mostly provided by airborne ice-penetrating radar, which samples data along the aerial vehicle's flight lines. Densely sampled coastal regions of Antarctica have flight lines separated by five to twenty kilometers, and data gaps in inland Antarctica can easily exceed fifty kilometers (Frémand and others, 2023).

These sparse bed elevation measurements must be interpolated to produce a gridded topographic map for ice sheet modeling applications (e.g. Herzfeld and others, 1993). In addition, the interpolated topography needs to satisfy physical laws that relate subglacial topography to other conditions. Specifically, the mass conservation equation relates subglacial topography to ice velocity, ice surface elevation, surface and basal mass balance, and change in ice thickness (Seroussi and others, 2011). Seroussi and others (2011) show that traditional interpolation methods, such as kriging, produce subglacial topographies that violate mass conservation when integrated with ice surface observations. This violation manifests as spurious, large-magnitude ice flux divergences, which can cause large and rapid changes in ice thickness in the first few time steps of the glacier simulation.

To find a physically realistic topography without the spurious ice flux, several methods have been proposed to constrain subglacial topography by mass conservation. These methods include numerically solving for bed topography from mass conservation (Morlighem and others, 2011; McNabb and others, 2012), using simplified glaciers model to invert subglacial topography and other parameters from ice velocity and surface elevation observations (e.g. Clarke and others, 2013; van Pelt and others, 2013; Perego and others, 2014), adopting machine learning to find an optimal topography that minimizes ice flux divergence (Teisberg and others, 2021), transferring perturbations from ice slab's base to its surface and solving the topography using either least square inversions or maximum a posteriori estimation (Gudmundsson, 2003; Pralong and Gudmundsson, 2011; Ockenden and others, 2023). These methods reconstruct physically realistic topographies compatible with ice surface measurements, which are valuable for modeling ice sheet evolution. Specifically, the method proposed in Morlighem and others (2011) has been used in BedMachine (Morlighem and others, 2017, 2020) to interpolate topography in fast-flowing regions of the Antarctic and Greenland Ice Sheets.

While the BedMachine estimate of subglacial topography in fast-flowing regions conserves ice mass, this solution to mass conservation has several limitations. First, the topography solution is often unrealistically smooth. Specifically, Morlighem and others (2011) solve for an optimized bed topography from mass conservation by regularizing the gradients of ice thickness. The topography is not required to match the spatial covariance structure in radar measurements (MacKie and others, 2021b) and is usually much smoother than the observed topography (Hoffman and others, 2022). Furthermore, the topographic error bound in Morlighem and others (2011) is calculated from the assumed error bound in observed ice velocity, surface and basal mass balance, and change in ice thickness. This topographic error represents how the optimal solution might be affected by variations of observational data within their error bounds, but it does not take into account the topographic uncertainty due to the non-uniqueness of solutions to mass conservation. In addition, the given error bound does not provide a direct way to propagate the topographic uncertainty to ice sheet simulation results and sea level projections. The uncertainty of non-unique solutions to mass conservation still needs to be robustly quantified, and the propagation of such uncertainty could be achieved through an ensemble of ice-sheet models initiated by equiprobable realizations of subglacial topography.

In contrast to deterministic interpolation approaches, geostatistical simulation is a class of interpolation methods that generates multiple realizations of the parameter field while preserving the parameter's spatial variability, which enables it to stochastically quantify uncertainty arising from sparse data. Several geostatistical methods have been used to simulate topographic realizations with realistic morphology and to quantify topographic uncertainty. For example, Zuo and others (2020) reconstruct subglacial topography using multiple-point statistics and revealed that subglacial water routing paths are highly sensitive to topographic uncertainty. In thermodynamic modeling of ice deformation, Law and others (2023) find that using topographies generated by sequential Gaussian simulation lead to enhanced ice deformation and a variable-thickness temperate ice layer at the base, which aligns more closely with borehole temperature observations. In contrast, the model with the BedMachine topography produces reduced ice deformation and a thin basal temperate ice layer.

Despite their ability to accurately quantify topographic uncertainty and preserve topographic roughness, traditional geostatistical methods do not constrain the topography by mass conservation and consequently could cause physical inconsistencies in ice flux. As a first step in addressing the issue, MacKie and others (2021b) employ a co-simulation technique in which topography is geostatistically simulated to correlate with mass-conserving topography from BedMachine (Morlighem and others, 2017). Although this approach visually aligns topographic realizations more closely with mass conservation constraints, it does not guarantee that ice mass is conserved, as the mass conservation equation is neither explicitly used nor proven to be satisfied in the workflow.

To reconcile the competing needs of imposing the mass conservation constraint, preserving realistic roughness, and measuring topographic uncertainty, we adopt a Markov chain Monte Carlo (MCMC) approach that integrates geostatistical simulations with mass conservation enforcement. MCMC is well-recognized as a sampling method used for model parameter inversion and uncertainty quantification (Gallagher and others, 2009). MCMC draws samples from the parameter distribution by iteratively updating the parameters and probabilistically accepting each update based on its probability density in the target distribution (Geyer, 2011). MCMC has previously been used to invert for mass-conserving subglacial topography, but the described algorithm was only demonstrated for a flowline of the glacier (Brinkerhoff and others, 2016) or relies on elevation-bands averaged quantities (Werder and others, 2020).

In other geoscience disciplines, geostatistics and geophysical inversion have been integrated through MCMC. For example, in the field of subsurface hydrology, geostatistical simulations are incorporated in the update step of MCMC. These geostatistical MCMC algorithms can invert for aquifer parameters while maintaining the parameter's spatial structure (Fu and Gómez-Hernández, 2008; Mariethoz and others, 2010; Reuschen and others, 2020). For instance, the MCMC algorithm developed by Hansen and others (2012) iteratively selects a random subset of parameters and re-generates them using geostatistics. This algorithm can stochastically generate parameter samples constrained by physics-based likelihoods and adhere to spatial covariance constraints. These experiments of integrating geostatistics and geophysical inversions inspire us to design an MCMC method for simulating subglacial topographies that are mass-conserving and have a realistic roughness.

In this study, we develop a novel MCMC method to produce an ensemble of subglacial topography realizations that conserve ice mass and preserve radar-measured topographic roughness. We apply our method to Denman Glacier, which is a major outlet glacier in the East Antarctic Ice Sheet with an annual ice discharge of $\sim$59.2 Gt from 2009 to 2017 (Rignot and others, 2019). BedMachine estimates the subglacial topography underneath Denman Glacier to be as deep as 3500 meters below sea level (Morlighem and others, 2020), where the location near the current grounding line exhibits a steep retrograde slope (Brancato and others, 2020). However, the shape and depth of the trough are not well-resolved in ice-penetrating radar, where the radar measurements at the center of the trough do not capture clear return signals from the bed (Liu and others, 2016; MacGregor and others, 2021). We choose this study area to test our method's ability to reconstruct mass-conserving topographic features with sparse radar measurements. In addition, the results could help future studies refine the uncertainty in Denman Glacier's projected evolution with a robust quantification of topographic uncertainty. To begin, we discuss the observational data used in the Data section. Next, in the Method section, we outline the workflow, review the key theories, and explore the implementation details. In the Results section, we quantitatively present the subglacial topography realizations sampled by the geostatistical MCMC. Finally, in the Discussion section, we describe the implications of the results and future applications.

DATA

The data used to reconstruct the subglacial topographies are presented in Fig. 1. We use MEaSUREs InSAR-Based Antarctica Ice Velocity Map version 2 (Rignot and others, 2017) for ice surface velocity, which is available at 450 m resolution. We obtain the surface mass balance by averaging the surface mass balance between 2014 and 2016 estimated by Regional Atmospheric Climate MOdel (RACMO2.3p2), which outputs at 27 km resolution (van Wessem and others, 2018). We obtain the surface elevation change rate by averaging the elevation change between May 2014 and May 2016 from MEaSUREs ITS_LIVE Antarctic Grounded Ice Sheet Elevation Change version 1 at 1.920 km resolution (Nilsson and others, 2023). We use ice surface elevation in BedMachine v3 at 500 m resolution (Morlighem and others, 2020), which is inferred from the Reference Elevation Model of Antarctica dataset (Howat and others, 2019). We also obtain the classification of regions (grounded ice/floating ice/open ocean/ice-free) from BedMachine at 500 m resolution. We project all data listed above onto a regular grid with 1 km resolution to match the topography resolution, for which we use spline interpolation for surface mass balance, nearest neighbor interpolation for region classification, and linear interpolation for other data. We compile bed elevation measurements from multiple datasets based on region classifications. In the grounded ice region, we use bed picks from ice-penetrating radar data assembled in Bedmap2 (Fretwell and others, 2013) and Bedmap3 (Frémand and others, 2023). Each cell in the grounded ice region is assigned the average bed elevation from the available radar measurements within that cell. If no measurements are available, the cell remains empty. In the following sections, the grid cells assigned with values are referred to as bed elevation measurements. Four different radar campaigns are used in the study region: the NASA Operation IceBridge campaign (MacGregor and others, 2021), the ICECAP campaign (Young and others, 2011; Blankenship and others, 2017), the ICECAP-EAGLE campaign (Young and others, 2016; Roberts and others, 2023), and the Talos-Dome campaign in 2003 (Bianchi and others, 2003). For regions classified as ice-free ocean, floating ice, and ice-free land, we project the BedMachine v3 bed elevation (Morlighem and others, 2020) from its 500 m grid to our 1 km grid using linear interpolation.

METHOD

Overview

We design three different MCMC chains to generate the ensemble of subglacial topography realizations (Fig. 2). We first run a preprocessing chain, which perturbs the initial topography by blocks of unconditional, spatially correlated random fields. The preprocessing chain allows perturbed topographies to have small-magnitude deviations from bed elevation measurements while constraining the magnitude of mass conservation residuals, which are the unresolved ice flux in the mass conservation equation. We use the results of the preprocessing chain to remove bed elevation measurements that could potentially be corrupted by radar clutter or erroneous bed picks. Then, we run 4 meso-scale chains that add blocks of perturbations to the topography while preserving the conditioning bed elevations. These perturbations enable changes in meso-scale ($\sim$10 km to $\sim$80 km) topographic features to reduce mass conservation residuals, but they do not guarantee that a realistic topographic roughness is preserved. Following each meso-scale chain, we run 10 fine-scale chains that use geostatistical simulation to reproduce fine-scale topographic features with a realistic roughness while constraining the magnitude of mass conservation residuals. The final topography

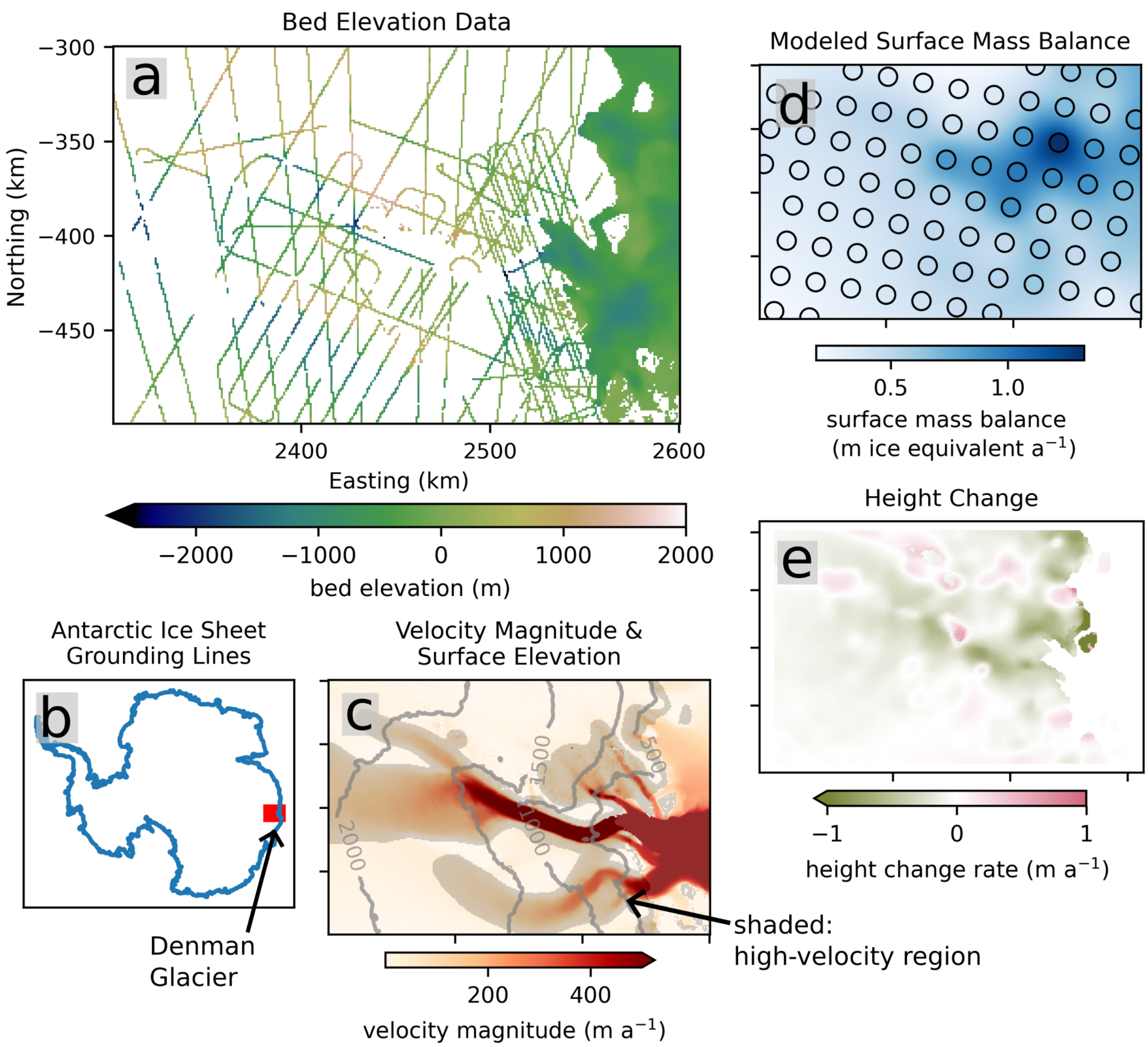

Fig. 1. (a) Gridded radar-measured bed elevations in Denman Glacier (Fretwell and others, 2013; Frémand and others, 2023; Morlighem and others, 2020), (b) Antarctic Ice Sheet grounding lines (Haran and others, 2018) and the study region, (c) ice surface speed (Rignot and others, 2017) overlaid by contour lines of the surface elevations (Howat and others, 2019), (d) spline-interpolated surface mass balance map overlaid by the original surface mass balance estimations (van Wessem and others, 2018) marked in black-edge circles, (e) linear-interpolated surface elevation change (Nilsson and others, 2023).

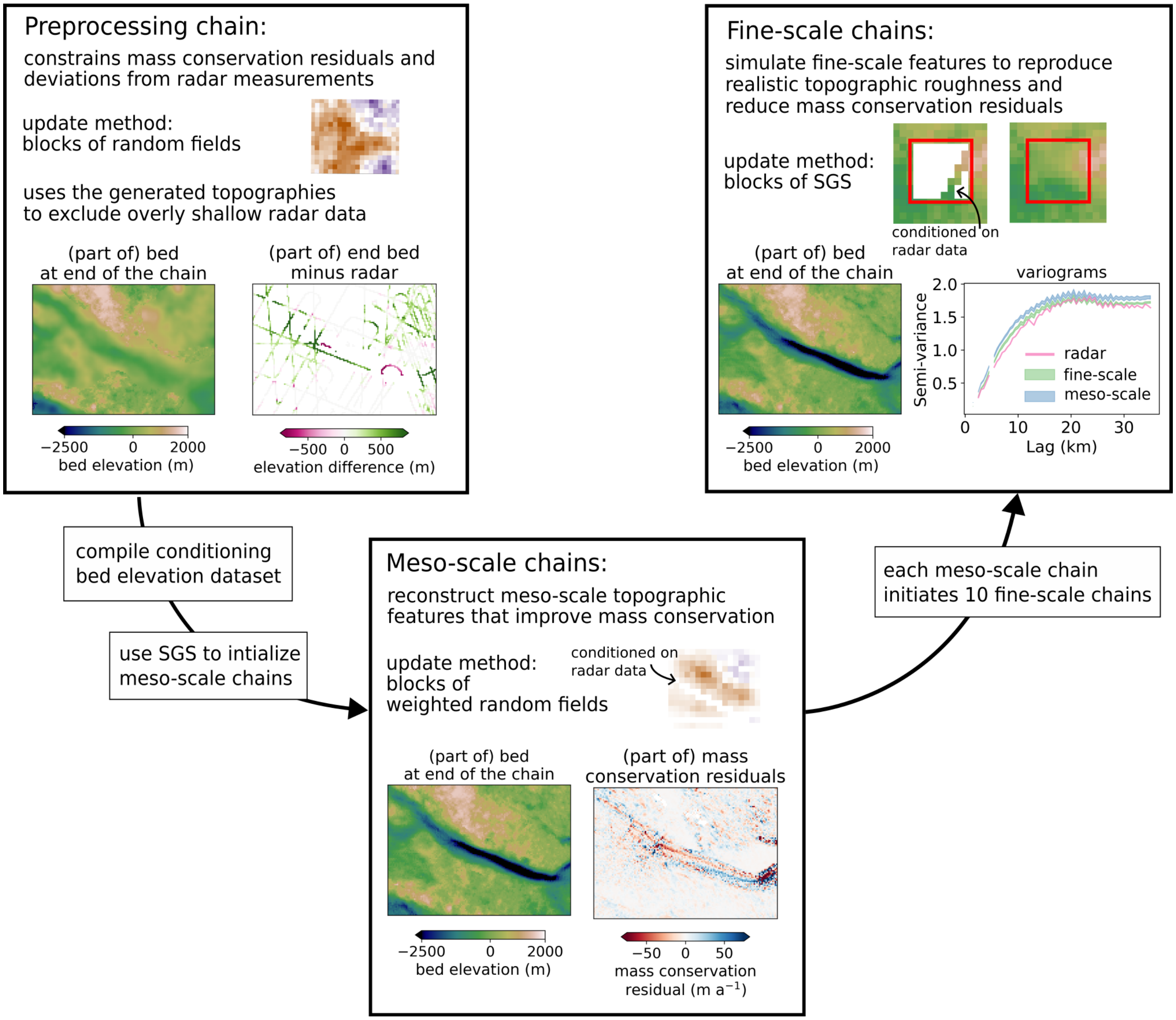

Fig. 2. Schematic overview of the workflow of the three MCMC chains.

ensemble consists of the topography realization at the end iteration of each fine-scale chain. In total, we run 4 meso-scale chains and 40 fine-scale chains, which generate an ensemble of 40 topography realizations.

In the following subsections, we first summarize key concepts in mass conservation, MCMC, and geostatistics and discuss how they are adapted for simulating subglacial topography. Then we describe the implementation details of the preprocess, meso-scale, and fine-scale chains. At the end, we outline how these chains are combined together to generate the topography ensemble.

Mass conservation: the physical constraint

Mass conservation can constrain the distribution of subglacial topography (e.g., Brinkerhoff and others, 2016) and ensure the compatibility of simulated topographies with other ice surface observations (Seroussi and others, 2011). The mass conservation equation (1) is derived by depth-integrating the ice continuity equation under the assumption of incompressible ice. The equation can relate high-resolution ice velocity to sparsely measured bed topography.

$$\frac{\partial H}{\partial t} = -\nabla \cdot (\bar{u}H) + \dot{M}_s + \dot{M}_b. \tag{1}$$

Here, $\frac{\partial H}{\partial t}$ is the rate of ice thickness change; $\nabla \cdot (\bar{u}H)$ is the depth-integrated ice flux divergence, which calculates the volume of ice entering and leaving an ice column from ice thickness, H, and depth-averaged velocity, $\bar{u}$. Surface processes, such as surface accumulation (positive) and surface ablation (negative), are represented by the surface mass balance, $\dot{M}_s$; whereas the basal mass balance, $\dot{M}_b$, includes basal accumulation (positive) and basal ablation (negative).

Further adjustments are made to tune this universal equation to the study region. The ice thickness is expressed as the difference between ice surface elevation and bed elevation. Since we consider the rate of ice thickness change in the unit of meters per year, we assume the annual change in bed elevation is negligible ($\frac{\partial H}{\partial t} = \frac{\partial (S-T)}{\partial t} \approx \frac{\partial S}{\partial t}$). As annual basal mass balance is estimated to be in centimeter-scale or smaller in the grounded ice region (e.g., Seroussi and others, 2019; McArthur and others, 2023), we approximate $\dot{M}_b$ as 0 following Seroussi and others (2011). Additionally, the depth-averaged velocity, $\bar{u}$, is approximated by surface velocity, u_s, which is a reasonable assumption in the high-velocity regions where basal sliding dominates. With the assumptions on $\bar{u}$ and M_b, we restrict the application of the method in fast-flowing, grounded ice regions. We compute a mask encompassing regions where the ice velocity is greater than or equal to 50 m a^{-1}. We smooth the edge of the mask by a mode filter of size 10 and then expand the mask outward for 5 km. Grid cells classified as open ocean, floating ice, and ice-free land are excluded from this region mask. This region (shown in Fig. 1(c)) is referred to as the high-velocity region and is where we apply the MCMC algorithm. We admit that the approximations made in the mass conservation equation could affect the final topography ensemble generated, and we further discuss the potential impact and future improvements in the discussion section.

After the adjustments, the mass conservation residual in the study region, which represents the ice flux divergence unresolved in the mass conservation equation, is defined as:

$$r = \nabla \cdot (u_s(S - T)) + \frac{\partial S}{\partial t} - \dot{M}_s. \tag{2}$$

MCMC and Bayes' theorem: topographic uncertainty quantification

MCMC is a well-established method for generating samples from a distribution that cannot be solved analytically (Gallagher and others, 2009). Often, Bayes' theorem provides a convenient framework to construct the probability density function of the distribution sampled by MCMC. To sample the distribution of subglacial topography, we denote topography as model parameters θ and denote ice surface velocity, surface mass balance, and rate of surface elevation change as data d. Bayes' theorem states that the distribution of model parameters conditioned on data is:

$$p(\theta|d) = \frac{p(d|\theta)p(\theta)}{p(d)}. \tag{3}$$

The posterior distribution $p(\theta|d)$ is inferred from a prior distribution $p(\theta)$, which is the probability of θ based on previous knowledge about subglacial bed elevations, and a likelihood $p(d|\theta)$, which is the probability of obtaining the observed data given a topography realization (Geyer, 2011). The prior distribution can be inferred from the differences l between the generated topography map and the bed elevation measurements. The likelihood is defined based on mass conservation residuals r.

$$p(\theta) = \exp\left(-\frac{\sum(l^2)}{2\sigma_l^2}\right). \tag{4}$$

$$p(d|\theta) = \exp\left(-\frac{\sum(r^2)}{2\sigma_r^2}\right). \tag{5}$$

Without a robust estimation of magnitude and spatial correlation of uncertainties in the observed data, the distributions of r and l are difficult to quantify analytically. In this study, we use BedMachine as a baseline of mass-conserving topography from which we define the target distribution. We approximate the distribution of r by fitting a Gaussian distribution on the mass conservation residuals from the BedMachine topography in the study region, for which we find the standard deviation σ_r to be 3 m a^{-1}. Similarly, the standard deviation of l, σ_l, is approximated by fitting a Gaussian distribution to the differences between the radar-measured bed elevations and the BedMachine topography in the study region, which is estimated

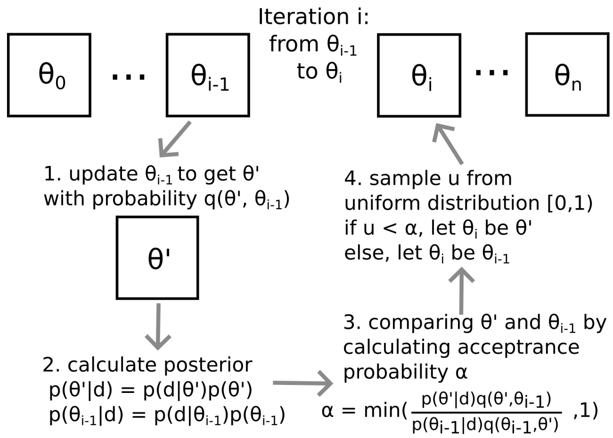

Fig. 3. A schematic diagram describing steps in one MCMC iteration. The topography θ' is (1) updated from θ_{i-1} and then (2,3) compared with θ_{i-1} based on their posteriors. Then (4) the MCMC probabilistically decides whether to keep θ' or keep θ_{i-1} as θ_i.

to be 80 meters.

The objective of MCMC is to approximate the posterior distribution by iteratively creating samples from the distribution in the form of a Markov chain. The chain is composed of a sequence of topography θ_i with $i \in 0, 1, 2, 3....$ Starting from the initial topography θ_0, each θ_i is generated at iteration i from θ_{i-1} with steps described in Fig. 3. The general equation for calculating acceptance probability α in Fig. 3 step 3 can be further simplified. The distribution $q(x, y)$ denotes the probability of obtaining x when updating y. In all three update methods, we can easily prove that $q(\theta', \theta_{i-1}) = q(\theta_{i-1}, \theta')$ for any θ' and any θ_{i-1} (see supplementary material section 1). Thus, $\alpha(\theta', \theta_{i-1}) = \min\left[\frac{p(\theta'|d)}{p(\theta_{i-1}|d)}, 1\right]$

By iteratively updating topography with the probability associated with the posterior distribution (Metropolis and others, 1953), MCMC effectively generates an ensemble of topography as samples from the posterior distribution. This ensemble of topography estimates bed elevation uncertainty constrained by both prior and likelihood, which are respectively informed by bed elevation measurements and mass conservation.

Geostatistics: realistic topographic roughness

Ice-penetrating radar measurements provide critical information about the spatial correlation of topographic features. This spatial correlation is visually presented as the roughness of the bed and can be quantified by a semi-variogram (i.e. variogram) (e.g. MacKie and others, 2021b), which is calculated by relating the distance between two elevation measurements to their value difference using equation (6) (Chilès and Delfiner, 2012):

$$\gamma(h) = \frac{1}{2N_h} \sum_{|u_i - u_j| \approx h} (Z(u_i) - Z(u_j))^2. \tag{6}$$

In equation (6), h is the separation distance; N_h is the number of data pairs separated by distance h; $Z(u)$ is the data value at the location u; and $\sum_{|u_i-u_j|\approx h}$ means summation for every pair of data points that are separated by h distance. When visualizing a variogram, $\gamma(h)$ usually increases with h until $\gamma(h)$ reaches a plateau. Intuitively, when two grid cells on the topography map are farther away (a larger h), their elevations are less correlated (a larger $\gamma(h)$) until they are far enough apart that the correlation vanishes ($\gamma(h)$ reaches a plateau). For a given h, a rougher subglacial topography will have larger bed elevation variations and thus a larger $\gamma(h)$. We utilize variograms to quantify and compare topographic roughness in generated topography realizations and radar measurements. All variograms are calculated using the SciKit-Gstats Python package with the Matheron estimator (Mälicke, 2022).

Sequential Gaussian Simulation (SGS) is a geostatistical simulation method that generates equally probable realizations of a random field while hard-conditioning the field to the conditioning data and reproducing the variogram statistics (Deutsch and Journel, 1997). When SGS is used for simulating subglacial topography, it reconstructs topographic realizations conditioned to the sparse radar measurements and reproduces the variogram of radar data (e.g. MacKie and others, 2021b). We take advantage of SGS to simulate realistically rough topographies in the fine-scale chains and to generate the initial topographies in the preprocessing chain and the meso-scale chains. We use the implementation of SGS in the GStatSim Python package (MacKie and others, 2023) and set the maximum number of nearest neighbors to 48 and the searching radius to 50 km.

Preprocessing chain: filter radar measurements

Ice-penetrating radar provides invaluable observations of the elevations of the subglacial bed. However, radar echoes near steep troughs are often incorrectly returned from off-nadir topographic high points, which leads to much shallower bed elevation measurements compared to the actual topography (Lapazaran and others, 2016; MacKie and others, 2021a). These misleading signals, known as clutter, can cause significant positive bias in the bed return signal recorded in the radargrams. In particular, the steep canyon at the Denman Glacier, which is estimated to be ∼3.5 km below sea level in the BedMachine dataset (Morlighem and others, 2020), creates a scenario where radargrams may easily be corrupted by clutter. If some radar-measured bed elevations in the study region are affected by clutter, they can restrict the simulated topography to a much shallower range of elevation, hindering the reduction of mass conservation residuals. While instrumental errors and error in estimated radio-wave velocity could also cause negative bias in the recorded bed elevations, these errors are usually in smaller magnitudes compared to clutters (Lapazaran and others, 2016). Thus, the preprocessing chain mainly considers the significant positive biases frequently arising from clutters.

To find and exclude potentially erroneous radar data, we run the preprocessing chain, which is an MCMC chain that allows generated topography to deviate from radar-measured bed elevations. We start this preprocessing chain with a topography that has a constant bed elevation value in the high-velocity region, SGS-generated topography in the rest of the grounded ice region, and topography from BedMachine in regions classified as floating ice, open ocean, or ice-free land.

In the preprocessing chain, we update the topography with blocks of spatially correlated perturbations, that is, blocks of unconditional random fields. These fields are sampled from zero-mean multivariate Gaussian distributions with an isotropic Gaussian covariance, which can be represented by a variogram with a zero nugget and a range sampled from a uniform distribution of [6 km, 60 km). The variogram range of the random fields determine the wavelength of topographic features produced, influencing the chain's convergence efficiency. However, it does not necessarily control the topographic roughness, as combining multiple random fields could produce perturbations in shorter or longer wavelengths. Thus, we provide a wide range of variogram range for the updates to randomly select from. To control the magnitudes of the perturbations, we multiply the random fields with a scaling factor, which is sampled from a uniform distribution of [50, 200). In addition, we restrict the updates by perturbing a rectangular block of topography at a time. Block-based update methods are often used to improve MCMC convergence when sampling high-dimensional distribution (Roberts and Sahu, 2002). Considering a large study area, perturbing all bed elevations at once will likely compensate favorable updates in one region with adverse updates in other regions, which leads to a low possibility for the update to be accepted. In contrast, perturbing bed elevations inside a randomly selected region improves acceptance rate. In each iteration, we randomly select a grid cell in the high-velocity region as the center of the block. The lateral dimensions of the block are randomly drawn from a uniform distribution of [50 km, 200 km). The topography outside of the high-velocity region is masked out and is not changed in every iteration.

At each iteration, the updated topography θ' is obtained by adding a block of random field to the topography from the last iteration θ_{i-1}. Then, these two topographies are evaluated by their probability densities in the posterior distribution. In this preprocessing chain, both deviations from the bed elevation measurements l and the mass conservation residuals r are used to calculate the posterior distribution. The acceptance probability is calculated as:

$$\begin{aligned}\alpha(x,y) &= \min\left[\frac{p(\theta')p(d|\theta')}{p(\theta_{i-1})p(d|\theta_{i-1})}, 1\right] \\ &= \min\left[\exp\left(-\frac{\sum(r'^2)-\sum(r_{i-1}^2)}{2\sigma_r^2} - \frac{\sum(l'^2)-\sum(l_{i-1}^2)}{2\sigma_l^2}\right), 1\right].\end{aligned} \tag{7}$$

After the chain converges, we calculate the mean topography of the last 4000 iterations, θ_p, and the mean standard deviation of l, $\hat{\sigma_l}$. To exclude data potentially corrupted by radar clutter, we remove radar measurements inside the high-velocity region that are at least $1.5\hat{\sigma_p}$ shallower than θ_p. An extra 10 grid cells of radar data near the deepest location of the Denman trough are also manually selected and discarded to avoid potential errors. In total, we remove 138 grid cells, consisting of ∼1.87% of the gridded radar measurements in the study area and ∼3.3% of the gridded radar measurements in the high-velocity region (Fig. S1). The remaining radar measurements are then assembled to be the conditioning data used in the next two MCMC chains.

Meso-scale chain: reconstruct large geometries

Large-scale bed geometries, including deep troughs, highlands, and mountain ranges, control the flow of ice and affect the distribution of mass conservation residuals. However, limited radar coverage may systematically fail to capture topographic features spanning tens or more kilometers. Furthermore, the sparse measurements might not sufficiently resolve the histogram of bed elevations. Therefore, before simulating fine-scale topographic features, it is necessary to first reconstruct the large-scale and meso-scale mass-conserving topographic features and find an approximation to the actual elevation distribution.

The meso-scale chain reduces the mass conservation residuals and preserves the conditioning bed elevations, and it does not require the simulated topography to match the observed elevation distribution. We initiate the meso-scale chain with an SGS-generated subglacial topography. Then, we update the initial topography by blocks of Weighted Random Fields (WRF), which are spatially correlated random perturbations with zero values at conditioning data locations. These WRF blocks are generated in three steps (Fig. 4). First, a block of topography is determined. The center of the block is randomly selected inside

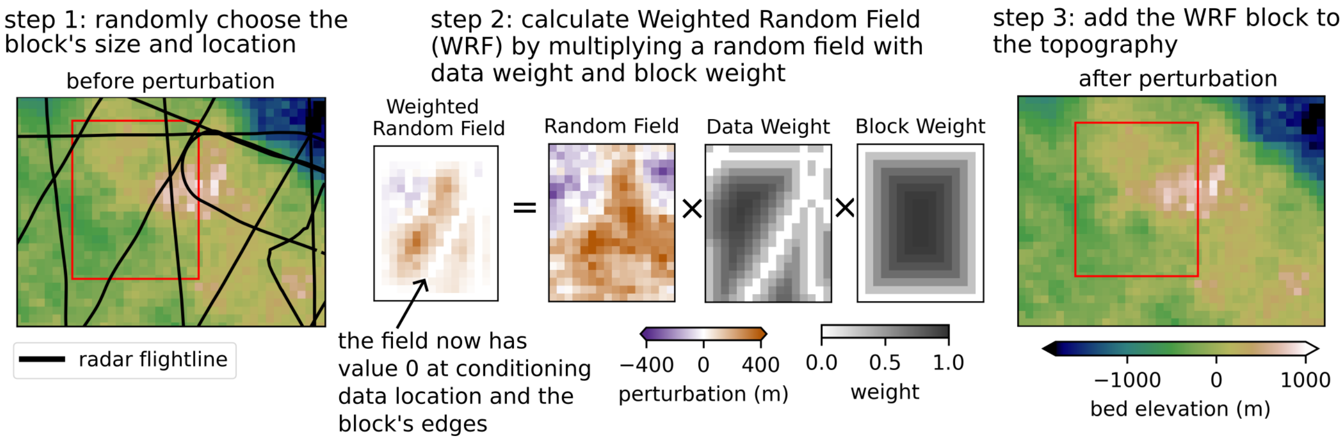

Fig. 4. An illustration of the update method used in the meso-scale chain. The red rectangle in step 1 and step 3 represent the selected random block.

the high-velocity region, and the block's lateral dimensions are sampled from a uniform distribution of [30 km, 70 km). Then, a random field with the same dimensions is generated. The random field is sampled from a multivariate Gaussian distribution with zero mean and an exponential, isotropic covariance model, which allows us to efficiently generate the field by Fourier Transform with the Python package GSTools (Müller and others, 2022). The covariance model can be represented by a variogram with zero nugget and a range randomly sampled from a uniform distribution of [18 km, 88 km) to encompass a wide range of perturbation length scales. We multiply the generated random field with a magnitude scaling factor sampled from a uniform distribution of [50, 200) to control the magnitude of the update and the acceptance rate. Then, we also multiply the field with the data weight matrix and the block weight matrix (see supplementary material section 2). The two weight matrices produce a WRF changing smoothly from value 0 at conditioning data locations and block's edges to the random field's values elsewhere. Finally, we add the WRF to the topography inside the block. The design of the WRF updates ensures that the updated topography does not change conditioning bed elevations and does not have abrupt jumps at the block's edges.

After updating the subglacial topography from the previous iteration θ_{i-1} to the new topography θ', we evaluate these two topographies by their probability densities in the posterior distribution. Since the conditioning bed elevations are not perturbed by WRF updates, we assume the prior distribution is equal ($p(\theta') = p(\theta_{i-1})$). The simplified acceptance probability in the meso-scale chain is:

$$\alpha(x,y) = \min\left[\frac{p(d|\theta')}{p(d|\theta_{i-1})}, 1\right] \\ = \min\left[\exp\left(-\frac{\sum(r'^2) - \sum(r_{i-1}^2)}{2\sigma_r^2}\right), 1\right], \tag{8}$$

where r' is the mass conservation residuals of topography θ' and r_{i-1} is the residuals of θ_{i-1}.

Fine-scale chain: simulate topographies with realistic roughness

Following the meso-scale chain, the fine-scale chain employs SGS to reconstruct realistically rough topographies while constraining the distribution of mass conservation residuals. To initialize the fine-scale chains, we first de-trend and normalize the topographies such that they resemble random fields with multivariate Gaussian distribution (Nowak and Verly, 2005; MacKie and others, 2023). We compute the topographic trend, θ_{trend}, by averaging topography realizations produced in the final segment of the meso-scale chain and smoothing the averaged map by a Gaussian filter kernel with a standard deviation of 5 km. We then sample a topography θ_f from the end of the meso-scale chain. We de-trend the topography by subtracting θ_{trend} from θ_f. The de-trended θ_f is then normal-score transformed using a Quantile Transformer Q. Finally, this de-trended, normalized θ_f is used to initiate one fine-scale chain.

In the next step, we calculate the variogram to represent the topographic roughness. We first subtract the conditioning bed elevations with θ_{trend}. Next, we normalize detrended conditioning data by the Quantile Transfer Q calculated from θ_f. The variogram of the normalized, de-trended conditioning data is then computed to represent the realistic topographic roughness.

Equipped with the variogram, the SGS-simulated topographies can reproduce the realistic topographic roughness observed in the conditioning data. However, while SGS simulates independent realizations, MCMC requires topography in iteration i to be derived from topography in iteration $i-1$. To satisfy the dependency requirement, each SGS simulation is restricted to a random rectangular block (Fig. 5) (e.g. Fu and Gómez-Hernández, 2008; Hansen and others, 2012; Laloy and others, 2016). In each MCMC iteration, we select the block's center at a random location in the high-velocity region and sample the block's lateral dimensions from a uniform distribution of [2 km, 8 km). Inside the block, we delete grid cells that are not conditioning data and then simulate the deleted grid cells using SGS. The simulation is conditioned on conditioning data inside the block and neighboring bed elevations outside of the block, which are generated

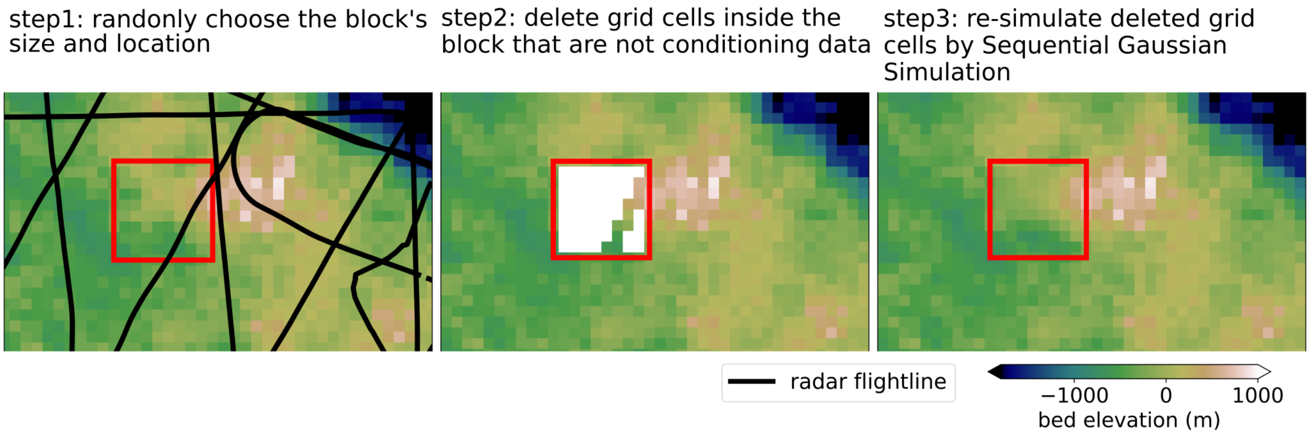

Fig. 5. An illustration of the update method used in the fine-scale chain. The red rectangle represents the selected random block.

in previous iterations. With the block update, the dependency requirement of MCMC is satisfied, and the SGS simulation ensures that the re-simulated topography inside the block is realistically rough.

To summarize, each iteration in the fine-scale chain consists of randomly selecting a block, simulating the normalized, de-trended topography inside the block by SGS, back-transforming the topography to the unit of meters, and then evaluating the updated topography through its probability density in the posterior distribution. By updating the topography with blocks of SGS in a Markov chain, the spatial covariance in subglacial topography is constrained and mass conservation is ensured. Because fine-scale chains generate updates that are conditioned to the conditioning bed elevations, the prior terms are equal ($p(\theta') = p(\theta_{i-1}) = 1$). The acceptance probability is calculated as in equation (9).

$$
\begin{aligned}
\alpha(x, y) &= \min\left[\frac{p(d|\theta')}{p(d|\theta_{i-1})}, 1\right] \\
&= \min\left[\exp\left(-\frac{\sum(r'^2) - \sum(r_{i-1}^2)}{2\sigma_r^2}\right), 1\right].
\end{aligned} \tag{9}
$$

Generate the topography ensemble

Both the meso-scale chains and fine-scale chains have unique advantages in simulating the subglacial topography realizations. Meso-scale chains reconstruct topographic features that are not captured in conditioning bed elevations but are critical for mass conservation. On the other hand, meso-scale chains are not required to reproduce the topographic roughness, implying that topographic features with unrealistic steep gradients could possibly be constructed for mass conservation. On the contrary, fine-scale chains simulate topography realizations with realistic roughness, but they perform better with a known bed elevation distribution and a known topography trend.

We designed a combination of meso-scale and fine-scale chains to generate an ensemble of topography realizations that are mass-conserving and realistically rough. First, we initiate 4 meso-scale chains with independent topographies simulated by SGS. Because the meso-scale chains do not perturb topography in the low-velocity region, initiating each chain with a different topography helps to account for topographic uncertainty in the low-velocity region. Each meso-scale chain first runs for 200,000 iterations, after which the large-scale topography is stable and the reduction in mass conservation residuals slows down. At the end of the 200,000th iteration, we visualize the autocorrelation of bed elevations and observe that the auto-correlations converge near zero before a lag of 4000 iterations (Fig. S2). The topographies generated between the 200,000th and 204,000th iterations are averaged and then smoothed by a Gaussian smoothing filter to find the topographic trend used in the fine-scale chain. After calculating the trend, each of the meso-scale chains continues for another 40,000 iterations to sample 10 topography realizations with a sampling interval of 4000 iterations.

Next, we initiate 10 fine-scale chains with each sampled topography realization. Each fine-cale chain runs for 200,000 iterations, after which $\sim$ 80% of the grid cells have been updated at least once. One topography realization is sampled at the end of each fine-scale chain. In total, 4 meso-scale chains diverge into 40 fine-scale chains, which provide an ensemble of 40 topography realizations.

RESULTS

We compare topographies described in BedMachine, produced by SGS, and generated by the geostatistical MCMC, with their respective mass conservation residuals at each grid cell in Fig. 6. Both MCMC and BedMachine construct a trough deeper than -3500 m beneath the main trunk of Denman Glacier, whereas SGS simulates bed elevations between -1000 to 0 m in the same location. Besides the overall similarity, we also observe different large-scale features in BedMachine and the MCMC-sampled topography. For instance, BedMachine shows a 2 km-deep, 30 km-long depression upstream of Denman Glacier, which does not exist in the MCMC-sampled topography.

Fig. 7 shows the sum of squares of mass conservation residuals in the 4 meso-scale chains and the corresponding 40 fine-scale chains. The bold lines highlight one meso-scale chain and one following fine-scale chain as examples. This meso-scale chain is initiated by the topography in Fig. 6(b) with large

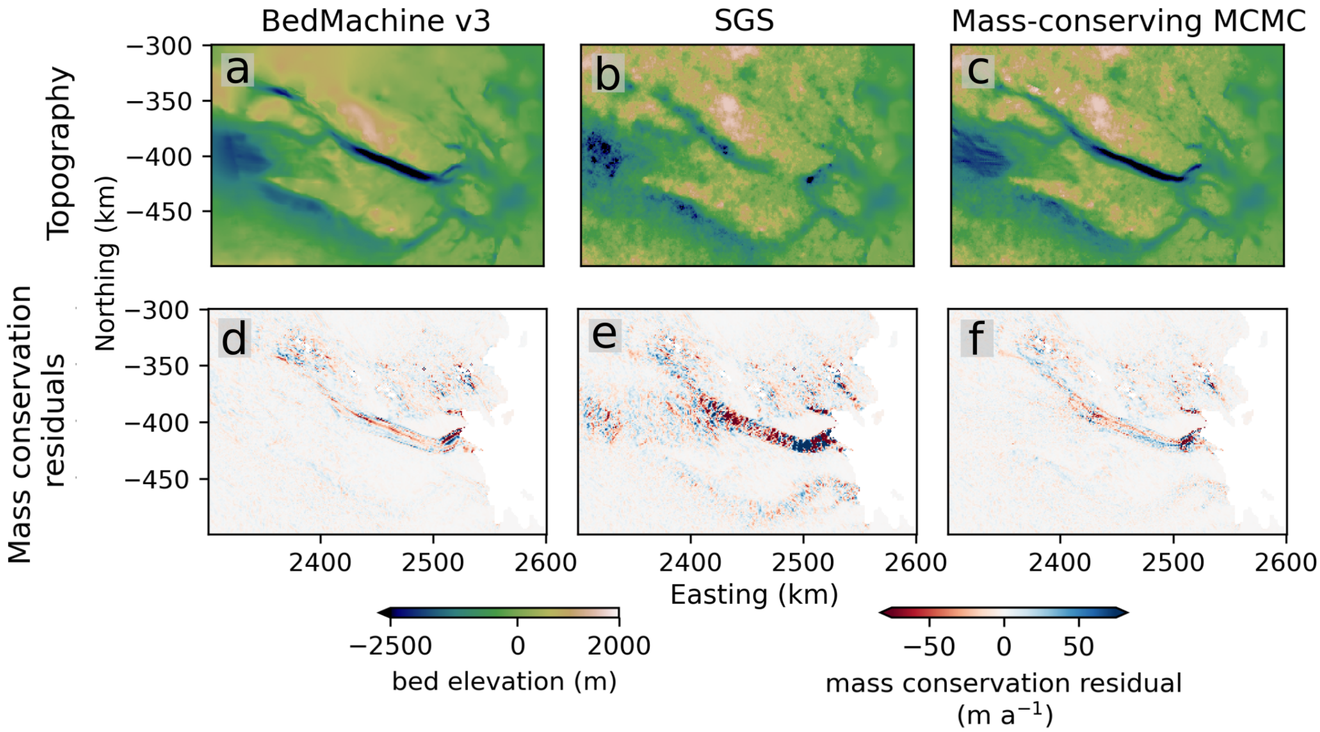

Fig. 6. (a,b,c) Topographies generated by different methods and (d,e,f) the associated mass conservation residuals.

mass conservation residuals concentrated in the Denman trough. After iterations of perturbation and simulations, the end topography in the fine-scale chain (Fig. 6(c)) reduced the residuals by one order of magnitude. The realizations assembled in the final ensemble, presented as orange dots in Fig. 7, have sums of squares of mass conservation residuals slightly lower than the one calculated for BedMachine.

We quantify and compare the topographic roughness by presenting the empirical variograms for the topographies in Fig. 8, where a higher semi-variance at the same lag distance indicates a rougher topography. The variogram of BedMachine topography has lower semi-variances compared to the variograms of radar-measured bed elevations, SGS-generated topography realizations, and members in the topography ensemble, whereas the latter three share similar semi-variances. The variograms from the 40 ensemble members have a small spread near the radar variogram with a slight bias toward higher semi-variance.

We present the mean and two standard deviations of the topography ensemble in Fig. 9(a) and Fig. 9(b). The ensemble mean shows the large-scale trend and some meso-scale topographic features that are consistent across different chains. The standard deviation has a mean of 45 meters and tends to be larger in areas with slower ice velocity, fewer radar flight lines, or near the boundary of the high-velocity region. Fig. 9(c) shows the differences between the ensemble mean topography and the BedMachine topography, which is less than 500 m across most areas but reaches 2000 m upstream of Denman Glacier. BedMachine provides

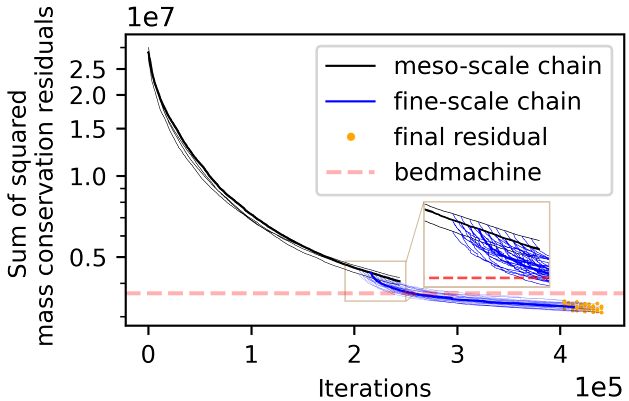

Fig. 7. The sum of squares of mass conservation residuals in the 4 meso-scale chains and the corresponding 40 fine-scale chains. The bold lines show an example of meso-scale chains and an example of fine-scale chains. The orange dots at the end of the lines denote the end sum of squared residuals of each topography realizations in the ensemble. The transition between meso-scale chains and fine-scale chains is enlarged in the inset figure.

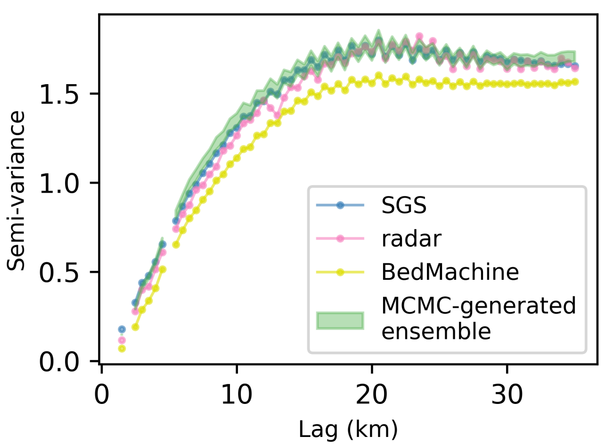

Fig. 8. Comparison of variograms calculated from de-trended, normalized BedMachine, SGS-generated, and MCMC-generated topographies in the high-velocity region and de-trended, normalized radar measurements in the entire study region. The trend used for de-trending is calculated by interpolating conditioning bed elevations through a radial basis function interpolator with a thin-plate-spline kernel. In the variogram calculation, we do not include the bed elevations in the narrow, deep Denman trough to avoid the artificial roughness added by bed elevations outside of the distribution of conditioning bed elevations.

the maximum error of bed elevation (Fig. 9(d)), which represents how the estimated maximum error in the ice velocity, surface mass balance, and surface elevation change could cause variations in the BedMachine topography solution. Comparing Fig. 9(c) and Fig. 9(d), we observe that the difference between the ensemble mean and BedMachine exceeds the BedMachine error bound, especially in the vicinity of the Denman trough.

To reveal the details of various topography realizations in the ensemble, we present several cross sections in the high-velocity region (Fig. 10 and Fig. 11). Fig. 10 shows the different geometry of the Denman trough reconstructed by MCMC and BedMachine, where the maximum difference exceeds 1 km. Among cross sections in Fig. 10, we observe that the spread of the bed elevation distribution changes across the region. The topography ensemble has a smaller spread within the trough (Fig. 10(c)) and upstream of the trough (Fig. 10(d)). In comparison, we find topographic uncertainty near the grounding line to be in several hundreds of meters (Fig. 10(e)). Fig. 11 provides cross sections over regions with relatively higher standard deviations. In the inland basin (Fig. 11(h)), the topography realizations diverge into two modes, where they share a similar large-scale geometry but differ by $\sim$500 m in elevation. On the other hand, at the cliff near the Denman trough (Fig. 11(i)), topography realizations resemble random perturbations added to the ensemble mean.

DISCUSSION

In this paper, we present a new geostatistical Markov chain Monte Carlo method and demonstrate its efficacy in sampling the subglacial bed elevation distribution of Denman Glacier. We show that the random perturbations in the meso-scale chains can reconstruct large topographic trends that minimize mass conservation residuals. We also show that blocks of geostatistical updates in the fine-scale chains can reproduce observed roughness in the simulated topographies. The end topography ensemble we generated validates the existence of a range of possible topographies that are mass-conserving, realistically rough, and constrained by radar-measured bed elevations.

The ensemble statistics and the cross sections (Fig. 9, Fig. 10, and Fig. 11) illustrate the potential of stochastic methods in sampling an ensemble of topographies and thus quantifying the topographic uncertainty. The sampled topography realizations have similar sums of squared mass conservation residuals (Fig. 7) while presenting distinct topographic features. The estimated topographic uncertainty is both substantial and spatially varying, with elevation differences ranging from 10^2 to 10^3 meters in different

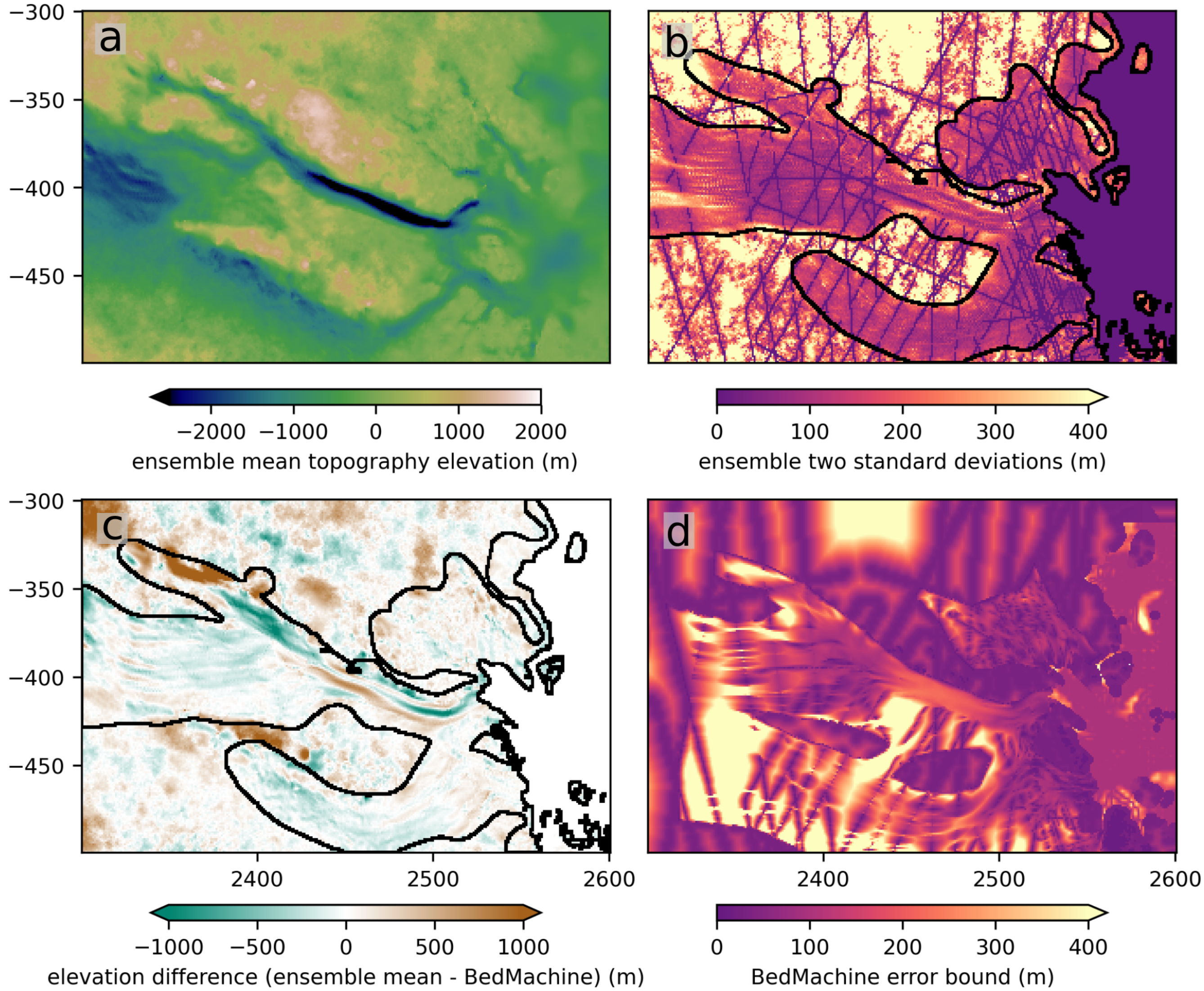

Fig. 9. (a) the ensemble mean bed elevation (m); (b) the ensemble standard deviation multiplied by two (m); (c) the elevation difference (ensemble mean - BedMachine; m); (d) the error bound of the BedMachine topography. The black outlines in (b) and (c) denote the high-velocity region, where the MCMC algorithm is applied

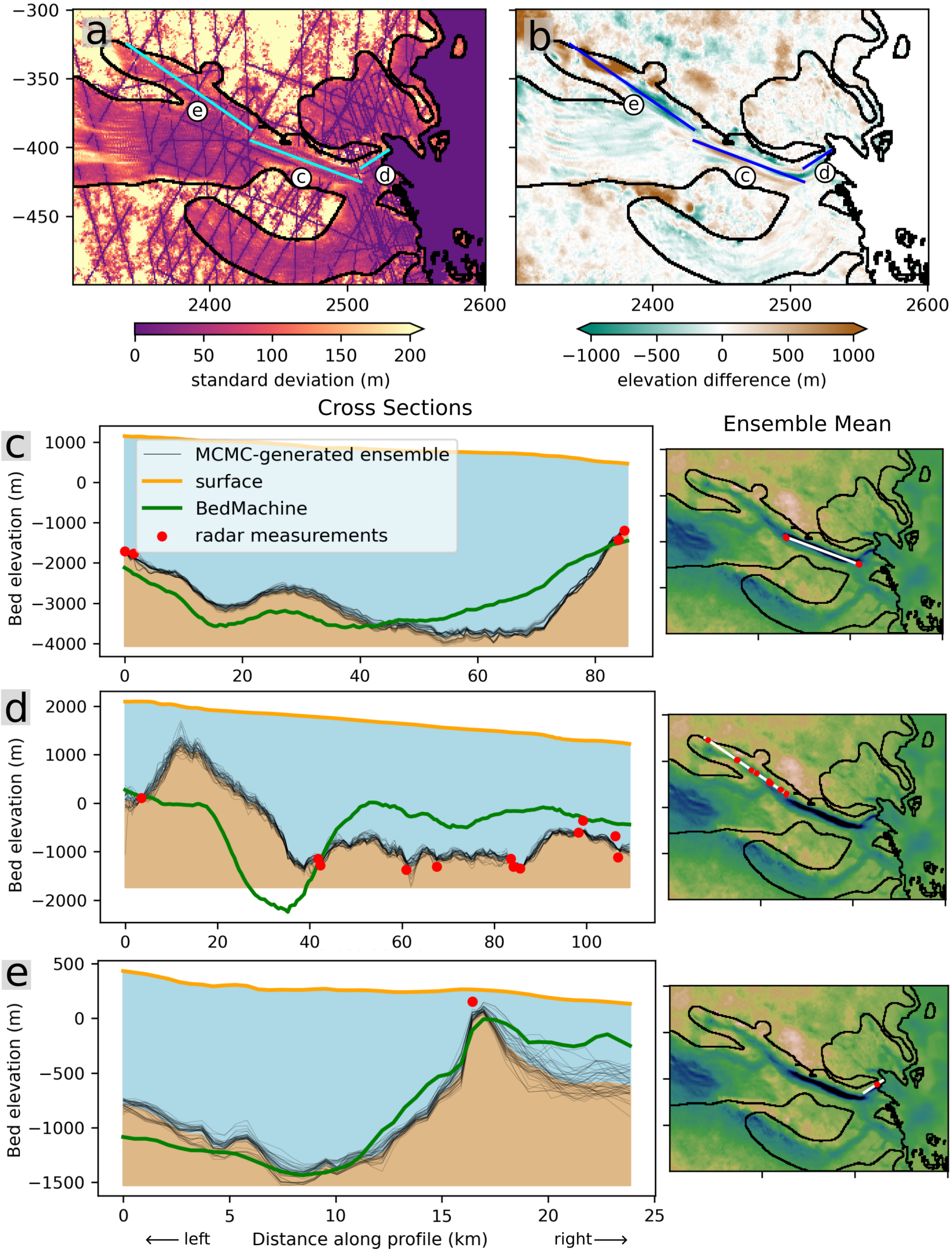

Fig. 10. Cross sections of the topography ensemble along Denman trough. The location of the transect lines, shown in blue lines, are plotted in the context of (a) ensemble standard deviation and (b) the difference between ensemble mean and BedMachine. The left column in (c), (d), and (e) show cross sections, and the right column show the location of transect lines. We use linear interpolation to project bed elevations from the gridded maps to the cross-sectional lines for better visualization. We use nearest neighbors interpolation to plot radar measurements on the cross sections.

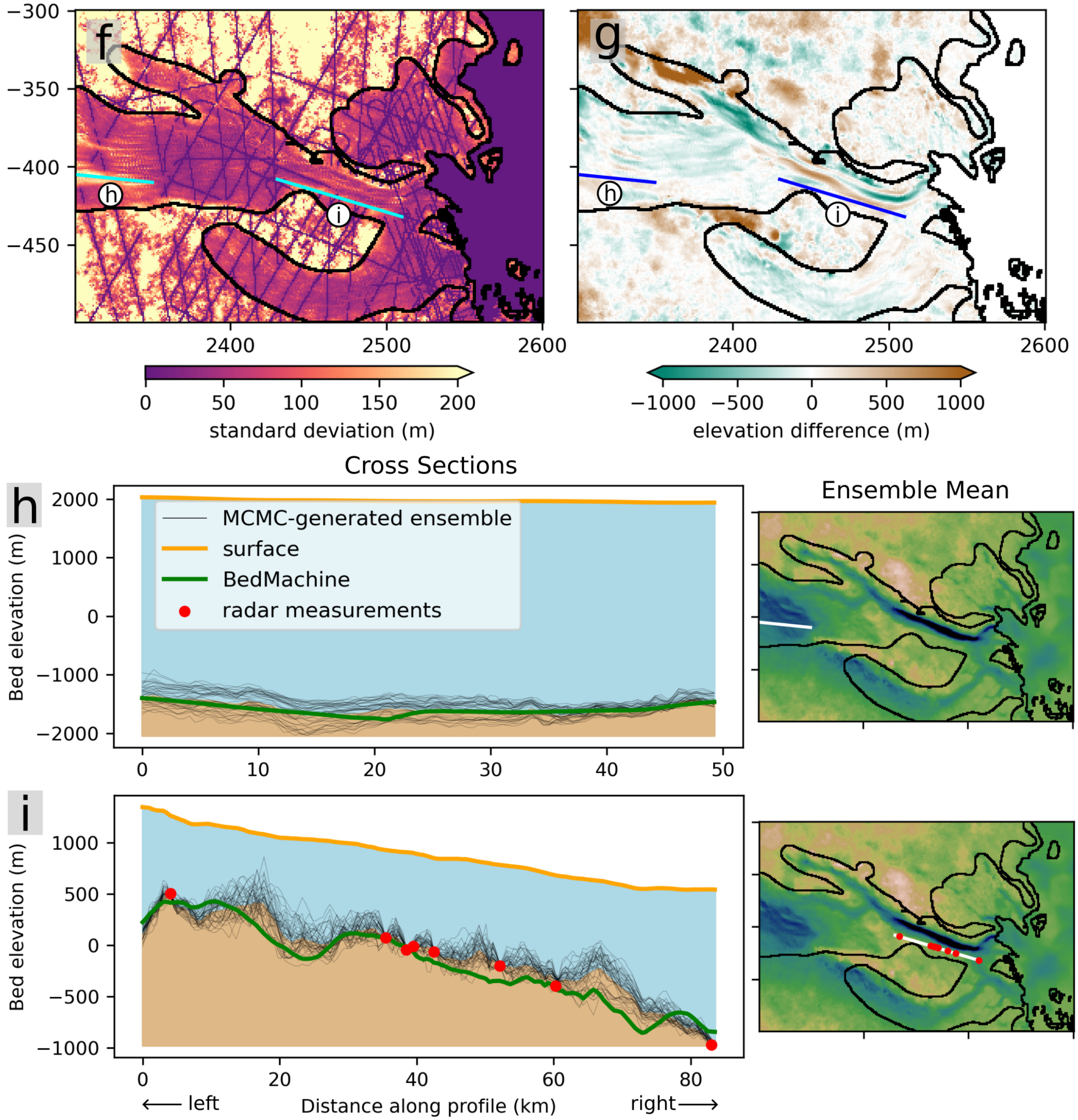

Fig. 11. Cross sections of the topography ensemble, where the transect lines go through two locations with high standard deviations. The layout and notations are similar to Fig. 10.

locations. The standard deviation of the topography ensemble across the Denman Glacier is shown in Fig. 9(b), and it tends to be larger in regions with lower ice velocity and sparser elevation measurements. We also observed that bed elevations in some regions exhibit unique distribution patterns, such as bi-modal distribution of bed elevation (Fig. 11(h)). This complex distribution, simulated by the MCMC algorithm, contrasts with the random topographic perturbations typically used to test the sensitivity of ice sheet models to bed topography (e.g. Sun and others, 2014; Castleman and others, 2022; Bulthuis and Larour, 2022; Wernecke and others, 2022). The diverse fine-scale topographic features generated in the MCMC, which can vary in elevation by up to 1200 m, could impact modeling of ice dynamics and highlight regions that should be prioritized for further data collections.

Subglacial topography is a critical component in many glacial processes, affecting ice deformation patterns (Meyer and Creyts, 2017; Law and others, 2023), subglacial water routing (Zuo and others, 2020; MacKie and others, 2021b), and stability of the glaciers (Gasson and others, 2015; Wernecke and others, 2022). The complex interactions between topographic uncertainty and ice stream dynamics can be studied via ensemble modeling, which is a well-established method for uncertainty propagation (e.g. Robel and others, 2019; Aschwanden and others, 2019; Albrecht and others, 2020; Bulthuis and others, 2019). The stochastic method we developed generates topography realizations that can be easily incorporated into an ensemble of models. The ability to propagate these significant topographic uncertainties to modeling results is critical for robustly quantifying sea level rise uncertainty, as found in a recent study on Thwaites Glacier (Castleman and others, 2022). Similarly, inversions of englacial and subglacial geophysical parameters, such as ice viscosity or sliding coefficient, often require a known bed topography. Most conventional inversions treat subglacial topography as a single deterministic map (Morlighem and others, 2010; Pollard and DeConto, 2012), which would cause the inversions to compensate errors in subglacial topography with values of inverted parameters (Kyrke-Smith and others, 2018; Hoffman and others, 2022; Rathmann and Lilien, 2022). An ensemble of topography realizations, such as the one simulated for Denman Glacier, can be used in an ensemble of inversions to explore how the inverted parameters compensate for topographic uncertainty. Additionally, the estimated bed elevation distribution is constrained by both mass conservation and the available radar measurements in the high-velocity region. The spatial distribution of the uncertainty could inform locations that need bed elevation measurements the most, thus possibly assisting the planning of future radar campaigns in ice-stream regions.

In Fig. 6, we observe the difference in topographies reconstructed by different methods. SGS reconstructs topography realizations based on the distribution of measured bed elevations; however, the sparsity of the flight lines may cause incomplete sampling of the distribution. On the other hand, both BedMachine and MCMC infer topography outside of the sampled elevation distribution to conserve ice mass, which leads the resulting topographies to have significantly different topographic trends compared to the SGS-generated realization. When comparing the large-scale bed geometry in the MCMC-generated ensemble and BedMachine, we find similarities in most regions but substantial differences along the Denman trough. These elevation differences could easily exceed the BedMachine-estimated error bound of bed elevation (Morlighem and others, 2020) (Fig. 9(c), 9(d)). Likewise, in some regions, the topography ensemble has a narrow spread that makes the BedMachine topography unlikely. This seemingly surprising observation can result from multiple factors. First, the MCMC method utilizes both a large-scale trend and fine-scale details to fit for mass conservation, whereas BedMachine solves for large-scale, smooth topographic features (Morlighem and others, 2020). The smoothness restriction could push the topography to a different solution space of mass conservation. Second, the MCMC-sampled topographies are hard conditioned on preprocessed radar data, whereas BedMachine allows deviations from radar data. Radar measurements not only restrict the local bed elevation but also could affect neighboring topography when combined with the mass conservation constraint. We suggest that future research could investigate the effect of soft-conditioning on radar data based on its uncertainty, potentially through approaches similar to the preprocessing chain or by geostatistical simulations with soft conditioning (e.g., Hansen and others, 2018).

The uncertainties and errors in observational data can affect the evaluations of mass conservation. Due to the limited spatial and temporal resolutions of observational data, we interpolate data from various resolutions onto the same grids and use ice velocity assembled across different times, whereas the mass conservation equation assumes synchronous data. Data uncertainties rising from the observational errors, the interpolations, and the differences in data collection time could change mass conservation residuals. Although we allow the mass conservation residuals to vary within a normal distribution approximated from the BedMachine topography, the variations in the residuals are not attributed to sources of uncertainties in each type of observational data. While improvements in data acquisition and processing could mitigate this problem, we suggest that several approaches might be able to directly incorporate data uncertainties in the MCMC method. Brinkerhoff and others (2016) adopt a MCMC method that infers ice velocity from the topography in each iteration and compares the inferred velocity with the observed velocity. This approach allows incorporating velocity uncertainty in the inversion of subglacial topography. However, the method was only demonstrated on a 2D flow line (Brinkerhoff and others, 2016) where velocity can be easily calculated from topography using mass conservation. Another approach is to treat observed data as random variables and perturb them in each MCMC iteration. In this way, the observational data and subglacial topography are jointly simulated and inverted, which significantly increases the computational cost and delays the Markov chain's convergence. We suggest that with a fast surrogate of ice stream models for calculating ice surface velocity (e.g. Jouvet and others, 2022) and advanced MCMC techniques designed for sampling high-dimensional parameters (e.g. Laloy and others, 2016; Reuschen and others, 2021), these possible solutions can be studied further. In addition, uncertainties caused by interpolation, such as the one experienced by surface mass balance, can be modeled through geostatistical approaches similar to MacKie and others (2021b) and Goovaerts (2001), which require comparatively less computational cost.

Our study also faces limitations similar to those in other studies that reconstruct topography based on mass conservation (e.g. Morlighem and others, 2011). Approximating basal mass balance as zero ignores its centimeter-scale variability, which could potentially affect the distribution of mass conservation residuals. Approximating the depth-averaged velocity from surface velocity - usually a reasonable assumption in fast flowing regions - ignores the changes in ice velocity with depth (McCormack and others, 2022). Future studies incorporating basal mass balance uncertainties could adopt similar approaches to those discussed in the previous paragraph. The depth-averaged velocity also can be modeled using a prior distribution based on a relationship between surface velocities and depth-averaged velocities. Then MCMC may iteratively sample the velocity's distribution to account for its uncertainty.

The variogram of bed elevations measured by radar provides a valuable constraint on the spatial covariance structure of simulated topography. On the other hand, topographic roughness and anisotropy of topographic features naturally vary based on the substrate's lithology and weathering process. In future studies, sub-regions with different topographic roughness and anisotropic angles can be partitioned, where different variograms could be used to simulate topography realizations with spatially varying roughness (e.g. MacKie and others, 2023). The flexibility of MCMC allows the multi-variogram approach to be easily incorporated into the current implementation of the method.

The computational expense of generating the topography ensemble can be alleviated using parallel computing and machine learning. In the current method, 40 topography realizations are obtained by running 4 meso-scale chains and 40 fine-scale chains in sequential order, which requires nearly two weeks of runtime. Because of the independence of these Markov chains, the runtime can be easily improved through parallelization of the chains. The number of topographies sampled in this parallel scheme theoretically could be independent of the nearly constant runtime and scale quasi-linearly with available computing resources. In addition, machine learning methods could be employed as time-efficient surrogates to generate geostatistical simulations (Laloy and others, 2018; Bai and Tahmasebi, 2022). Considering that SGS is the most time-consuming component in the current method, adopting machine learning to approximate the geostatistical simulations could further shorten the runtime.

CONCLUSION

Reconstructing subglacial topography from sparse radar measurements faces difficulties in preserving realistic topographic roughness and ensuring physical consistency with surface observations. In this study, we develop a novel geostatistical MCMC method for stochastically simulating subglacial topography and test the method on Denman Glacier. We successfully simulate an ensemble of mass-conserving, realistically rough, and radar-constrained topography realizations. The simulated topographies show large differences to the numerically solved topography in BedMachine. The topography ensemble also presents spatially varying topographic uncertainty and distinct meso-scale and fine-scale topographic features across realizations. We demonstrated the application of geostatistical MCMC in the inversion of subglacial topography. Furthermore, the topography ensemble generated provides an opportunity to quantify the impact of topographic uncertainty on ice sheet modeling and sea-level-rise projections.

DATA AVAILABILITY

The simulated topography ensemble that support the findings of this study is openly available in U.S. Antarctic Program Data Center, which can be found at https://doi.org/10.15784/601927.

SUPPLEMENTARY MATERIAL

The supplementary material is attached in the submission.

COMPETING INTERESTS

The authors have no competing interests to declare

ACKNOWLEDGMENT

N.S., E.J.M., and M.J.F. were supported by NSF award 2324092. N.S. was also supported by the research fellowship under Department of Geological Sciences, University of Florida. F.S.M. was supported under an Australian Research Council (ARC) Discovery Early Career Research Award (DECRA; DE210101433) and the ARC Special Research Initiative Securing Antarctica's Environmental Future (SR200100005).

REFERENCES

Albrecht T, Winkelmann R and Levermann A (2020) Glacial-cycle simulations of the antarctic ice sheet with the parallel ice sheet model (pism) – part 2: Parameter ensemble analysis. *The Cryosphere*, **14**(2), 633–656 (doi: 10.5194/tc-14-633-2020)

Aschwanden A, Fahnestock MA, Truffer M, Brinkerhoff DJ, Hock R, Khroulev C, Mottram R and Khan SA (2019) Contribution of the greenland ice sheet to sea level over the next millennium. *Science Advances*, **5**(6), eaav9396 (doi: 10.1126/sciadv.aav9396)

Bai T and Tahmasebi P (2022) Sequential gaussian simulation for geosystems modeling: A machine learning approach. *Geoscience Frontiers*, **13**(1), 101258 (doi: https://doi.org/10.1016/j.gsf.2021.101258)

Bianchi C, Cafarella L, De Michelis P, Forieri A, Frezzotti M, Tabacco IE and Zirizzotti A (2003) Radio echo sounding (res) investigations at talos dome (east antarctica): bedrock topography and ice thickness. *Annals of Geophysics*, **46**(6), 1265–1270 (doi: doi.org/10.4401/ag-3471)

Bingham RG, Vaughan DG, King EC, Davies D, Cornford SL, Smith AM, Arthern RJ, Brisbourne AM, De Rydt J, Graham AGC, Spagnolo M, Marsh OJ and Shean DE (2017) Diverse landscapes beneath pine island glacier influence ice flow. *Nature Communications*, **8**(1) (doi: 10.1038/s41467-017-01597-y)

Blankenship D, Kempf S, Young D, Richter T, Schroeder D, Greenbaum J, van Ommen T, Warner R, Roberts J, Young N, Lemeur E, Siegert M and Holt J (2017) Icebridge hicars 1 l1b time-tagged echo strength profiles, version 1 (doi: 10.5067/W2KXX0MYNJ9G)

Bradwell T, Small D, Fabel D, Smedley RK, Clark CD, Saher MH, Callard SL, Chiverrell RC, Dove D, Moreton SG, Roberts DH, Duller GAT and Cofaigh CO (2019) Ice-stream demise dynamically conditioned by trough shape and bed strength. *Science Advances*, **5**(4) (doi: 10.1126/sciadv.aau1380)

Brancato V, Rignot E, Milillo P, Morlighem M, Mouginot J, An L, Scheuchl B, Jeong S, Rizzoli P, Bueso Bello JL and Prats-Iraola P (2020) Grounding line retreat of denman glacier, east antarctica, measured with cosmo-skymed radar interferometry data. *Geophysical Research Letters*, **47**(7), e2019GL086291 (doi: https://doi.org/10.1029/2019GL086291)

Brinkerhoff DJ, Aschwanden A and Truffer M (2016) Bayesian Inference of Subglacial Topography Using Mass Conservation. *Frontiers in Earth Science*, **4** (doi: 10.3389/feart.2016.00008)

Bulthuis K and Larour E (2022) Implementation of a gaussian markov random field sampler for forward uncertainty quantification in the ice-sheet and sea-level system model v4.19. *Geoscientific Model Development*, **15**(3), 1195–1217 (doi: 10.5194/gmd-15-1195-2022)

Bulthuis K, Arnst M, Sun S and Pattyn F (2019) Uncertainty quantification of the multi-centennial response of the antarctic ice sheet to climate change. *The Cryosphere*, **13**(4), 1349–1380 (doi: 10.5194/tc-13-1349-2019)

Castleman BA, Schlegel NJ, Caron L, Larour E and Khazendar A (2022) Derivation of bedrock topography measurement requirements for the reduction of uncertainty in ice-sheet model projections of thwaites glacier. *The Cryosphere*, **16**(3), 761–778 (doi: 10.5194/tc-16-761-2022)

Chilès JP and Delfiner P (2012) *Geostatistics : Modeling Spatial Uncertainty*. John Wiley & Sons, Incorporated, Newark, 2 edition, ISBN 9781118136188 (doi: 10.1002/9781118136188)

Clarke GKC, Anslow FS, Jarosch AH, Radić V, Menounos B, Bolch T and Berthier E (2013) Ice Volume and Subglacial Topography for Western Canadian Glaciers from Mass Balance Fields, Thinning Rates, and a Bed Stress Model. *Journal of Climate*, **26**(12), 4282–4303 (doi: 10.1175/JCLI-D-12-00513.1)

Colgan W, MacGregor JA, Mankoff KD, Haagenson R, Rajaram H, Martos YM, Morlighem M, Fahnestock MA and Kjeldsen KK (2021) Topographic correction of geothermal heat flux in greenland and antarctica. *Journal of Geophysical Research: Earth Surface*, **126**(2), e2020JF005598 (doi: https://doi.org/10.1029/2020JF005598)

Deutsch CV and Journel AG (1997) *GSLIB: Geostatistical Software Library and User's Guide*. Oxford University Press, New York, 2 edition

Frémand AC, Fretwell P, Bodart JA, Pritchard HD, Aitken A, Bamber JL, Bell R, Bianchi C, Bingham RG, Blankenship DD, Casassa G, Catania G, Christianson K, Conway H, Corr HFJ, Cui X, Damaske D, Damm V, Drews R, Eagles G, Eisen O, Eisermann H, Ferraccioli F, Field E, Forsberg R, Franke S, Fujita S, Gim Y, Goel V, Gogineni SP, Greenbaum J, Hills B, Hindmarsh RCA, Hoffman AO, Holmlund P, Holschuh N, Holt JW, Horlings AN, Humbert A, Jacobel RW, Jansen D, Jenkins A, Jokat W, Jordan T, King E, Kohler J, Krabill W, Kusk Gillespie M, Langley K, Lee J, Leitchenkov G, Leuschen C, Luyendyk B, MacGregor J, MacKie E, Matsuoka K, Morlighem M, Mouginot J, Nitsche FO, Nogi Y, Nost OA, Paden J, Pattyn F, Popov SV, Rignot E, Rippin DM, Rivera A, Roberts J, Ross N, Ruppel A, Schroeder DM, Siegert MJ, Smith AM, Steinhage D, Studinger M, Sun B, Tabacco

I, Tinto K, Urbini S, Vaughan D, Welch BC, Wilson DS, Young DA and Zirizzotti A (2023) Antarctic bedmap data: Findable, accessible, interoperable, and reusable (fair) sharing of 60 years of ice bed, surface, and thickness data. *Earth System Science Data*, **15**(7), 2695–2710 (doi: 10.5194/essd-15-2695-2023)

Fretwell P, Pritchard HD, Vaughan DG, Bamber JL, Barrand NE, Bell R, Bianchi C, Bingham RG, Blankenship DD, Casassa G, Catania G, Callens D, Conway H, Cook AJ, Corr HFJ, Damaske D, Damm V, Ferraccioli F, Forsberg R, Fujita S, Gim Y, Gogineni P, Griggs JA, Hindmarsh RCA, Holmlund P, Holt JW, Jacobel RW, Jenkins A, Jokat W, Jordan T, King EC, Kohler J, Krabill W, Riger-Kusk M, Langley KA, Leitchenkov G, Leuschen C, Luyendyk BP, Matsuoka K, Mouginot J, Nitsche FO, Nogi Y, Nost OA, Popov SV, Rignot E, Rippin DM, Rivera A, Roberts J, Ross N, Siegert MJ, Smith AM, Steinhage D, Studinger M, Sun B, Tinto BK, Welch BC, Wilson D, Young DA, Xiangbin C and Zirizzotti A (2013) Bedmap2: improved ice bed, surface and thickness datasets for antarctica. *The Cryosphere*, **7**(1), 375–393 (doi: 10.5194/tc-7-375-2013)

Fu J and Gómez-Hernández JJ (2008) Preserving spatial structure for inverse stochastic simulation using blocking Markov chain Monte Carlo method. *Inverse Problems in Science and Engineering*, **16**(7), 865–884 (doi: 10.1080/17415970802015781)

Gallagher K, Charvin K, Nielsen S, Sambridge M and Stephenson J (2009) Markov chain Monte Carlo (MCMC) sampling methods to determine optimal models, model resolution and model choice for Earth Science problems. *Marine and Petroleum Geology*, **26**(4), 525–535 (doi: 10.1016/j.marpetgeo.2009.01.003)

Gasson E, DeConto R and Pollard D (2015) Antarctic bedrock topography uncertainty and ice sheet stability. *Geophysical Research Letters*, **42**(13), 5372–5377 (doi: https://doi.org/10.1002/2015GL064322)

Geyer CJ (2011) Introduction to markov chain monte carlo. In S Brooks, A Gelman, G Jones and XL Meng (eds.), *Handbook of Markov Chain Monte Carlo*, 3–48, Chapman and Hall/CRC, New York, ISBN 9780429138508 (doi: 10.1201/b10905)

Goovaerts P (2001) Geostatistical modelling of uncertainty in soil science. *Geoderma*, **103**(1), 3–26 (doi: https://doi.org/10.1016/S0016-7061(01)00067-2)

Gudmundsson GH (2003) Transmission of basal variability to a glacier surface. *Journal of Geophysical Research: Solid Earth*, **108**(B5) (doi: https://doi.org/10.1029/2002JB002107)

Hansen TM, Cordua KS and Mosegaard K (2012) Inverse problems with non-trivial priors: efficient solution through sequential gibbs sampling. *Computational Geosciences*, **16**(3), 593–611

Hansen TM, Vu LT, Mosegaard K and Cordua KS (2018) Multiple point statistical simulation using uncertain (soft) conditional data. *Computers & Geosciences*, **114**, 1–10 (doi: https://doi.org/10.1016/j.cageo.2018.01.017)

Haran T, Klinger M, Bohlander J, Fahnestock M, Painter T and Scambos T (2018) Measures modis mosaic of antarctica 2013-2014 (moa2014) image map, version 1 (doi: 10.5067/RNF17BP824UM)

Herzfeld UC, Eriksson MG and Holmlund P (1993) On the influence of kriging parameters on the cartographic output—a study in mapping subglacial topography. *Mathematical Geology*, **25**(7), 881–900 (doi: 10.1007/BF00891049)

Hoffman AO, Christianson K, Holschuh N, Case E, Kingslake J and Arthern R (2022) The impact of basal roughness on inland thwaites glacier sliding. *Geophysical Research Letters*, **49**(14) (doi: https://doi.org/10.1029/2021GL096564)

Howat IM, Porter C, Smith BE, Noh MJ and Morin P (2019) The reference elevation model of antarctica. *The Cryosphere*, **13**(2), 665–674 (doi: 10.5194/tc-13-665-2019)

Jouvet G, Cordonnier G, Kim B, Lüthi M, Vieli A and Aschwanden A (2022) Deep learning speeds up ice flow modelling by several orders of magnitude. *Journal of Glaciology*, **68**(270), 651–664 (doi: 10.1017/jog.2021.120)

Kyrke-Smith TM, Gudmundsson GH and Farrell PE (2018) Relevance of detail in basal topography for basal slipperiness inversions: A case study on pine island glacier, antarctica. *Frontiers in Earth Science*, **6** (doi: 10.3389/feart.2018.00033)

Laloy E, Linde N, Jacques D and Mariethoz G (2016) Merging parallel tempering with sequential geostatistical resampling for improved posterior exploration of high-dimensional subsurface categorical fields. *Advances in Water Resources*, **90**, 57–69 (doi: https://doi.org/10.1016/j.advwatres.2016.02.008)

Laloy E, Hérault R, Jacques D and Linde N (2018) Training-image based geostatistical inversion using a spatial generative adversarial neural network. *Water Resources Research*, **54**(1), 381–406 (doi: https://doi.org/10.1002/2017WR022148)

Lapazaran JJ, Otero J, Martín-Español A and Navarro FJ (2016) On the errors involved in ice-thickness estimates i: ground-penetrating radar measurement errors. *Journal of Glaciology*, **62**(236), 1008–1020 (doi: 10.1017/jog.2016.93)

Law R, Christoffersen P, MacKie E, Cook S, Haseloff M and Gagliardini O (2023) Complex motion of Greenland Ice Sheet outlet glaciers with basal temperate ice. *Science Advances*, **9**(6), eabq5180 (doi: 10.1126/sciadv.abq5180)

Liu W, Purdon K, Stafford T, Paden J and Li X (2016) Open polar server (ops)—an open source infrastructure for the cryosphere community. *ISPRS International Journal of Geo-Information*, **5**(3) (doi: 10.3390/ijgi5030032)

MacGregor JA, Boisvert LN, Medley B, Petty AA, Harbeck JP, Bell RE, Blair JB, Blanchard-Wrigglesworth E, Buckley EM, Christoffersen MS, Cochran JR, Csathó BM, De Marco EL, Dominguez RT, Fahnestock MA, Farrell

SL, Gogineni SP, Greenbaum JS, Hansen CM, Hofton MA, Holt JW, Jezek KC, Koenig LS, Kurtz NT, Kwok R, Larsen CF, Leuschen CJ, Locke CD, Manizade SS, Martin S, Neumann TA, Nowicki SMJ, Paden JD, Richter-Menge JA, Rignot EJ, Rodríguez-Morales F, Siegfried MR, Smith BE, Sonntag JG, Studinger M, Tinto KJ, Truffer M, Wagner TP, Woods JE, Young DA and Yungel JK (2021) The scientific legacy of nasa's operation icebridge. *Reviews of Geophysics*, **59**(2), e2020RG000712 (doi: https://doi.org/10.1029/2020RG000712)

MacKie EJ, Schroeder DM, Steinbrügge G and Culberg R (2021a) Quantifying spatial relationships in ice penetrating radar measurement uncertainty through clutter simulation. In *2021 IEEE International Geoscience and Remote Sensing Symposium IGARSS*, 8688–8691 (doi: 10.1109/IGARSS47720.2021.9553045)

MacKie EJ, Schroeder DM, Zuo C, Yin Z and Caers J (2021b) Stochastic modeling of subglacial topography exposes uncertainty in water routing at jakobshavn glacier. *Journal of Glaciology*, **67**(261), 75–83 (doi: 10.1017/jog.2020.84)

MacKie EJ, Field M, Wang L, Yin Z, Schoedl N, Hibbs M and Zhang A (2023) GStatSim V1.0: a Python package for geostatistical interpolation and conditional simulation. *Geoscientific Model Development*, **16**(13), 3765–3783 (doi: 10.5194/gmd-16-3765-2023)

Mälicke M (2022) Scikit-gstat 1.0: a scipy-flavored geostatistical variogram estimation toolbox written in python. *Geoscientific Model Development*, **15**(6), 2505–2532 (doi: 10.5194/gmd-15-2505-2022)

Mariethoz G, Renard P and Caers J (2010) Bayesian inverse problem and optimization with iterative spatial resampling. *Water Resources Research*, **46**(11), ISSN 1944-7973 (doi: 10.1029/2010WR009274)

McArthur K, McCormack FS and Dow CF (2023) Basal conditions of denman glacier from glacier hydrology and ice dynamics modeling. *The Cryosphere*, **17**(11), 4705–4727 (doi: 10.5194/tc-17-4705-2023)

McCormack FS, Warner RC, Seroussi H, Dow CF, Roberts JL and Treverrow A (2022) Modeling the deformation regime of thwaites glacier, west antarctica, using a simple flow relation for ice anisotropy (estar). *Journal of Geophysical Research: Earth Surface*, **127**(3), e2021JF006332 (doi: https://doi.org/10.1029/2021JF006332)

McNabb RW, Hock R, O'Neel S, Rasmussen LA, Ahn Y, Braun M, Conway H, Herreid S, Joughin I, Pfeffer WT and et al (2012) Using surface velocities to calculate ice thickness and bed topography: a case study at columbia glacier, alaska, usa. *Journal of Glaciology*, **58**(212), 1151–1164 (doi: 10.3189/2012JoG11J249)

Metropolis N, Rosenbluth AW, Rosenbluth MN, Teller AH and Teller E (1953) Equation of State Calculations by Fast Computing Machines. *The Journal of Chemical Physics*, **21**(6), 1087–1092 (doi: 10.1063/1.1699114)

Meyer CR and Creyts TT (2017) Formation of ice eddies in subglacial mountain valleys. *Journal of Geophysical Research: Earth Surface*, **122**(9), 1574–1588 (doi: https://doi.org/10.1002/2017JF004329)

Morlighem M, Rignot E, Seroussi H, Larour E, Ben Dhia H and Aubry D (2010) Spatial patterns of basal drag inferred using control methods from a full-stokes and simpler models for pine island glacier, west antarctica. *Geophysical Research Letters*, **37**(14) (doi: https://doi.org/10.1029/2010GL043853)

Morlighem M, Rignot E, Seroussi H, Larour E, Ben Dhia H and Aubry D (2011) A mass conservation approach for mapping glacier ice thickness. *Geophysical Research Letters*, **38**(19) (doi: 10.1029/2011GL048659)

Morlighem M, Williams CN, Rignot E, An L, Arndt JE, Bamber JL, Catania G, Chauché N, Dowdeswell JA, Dorschel B, Fenty I, Hogan K, Howat I, Hubbard A, Jakobsson M, Jordan TM, Kjeldsen KK, Millan R, Mayer L, Mouginot J, Noël BPY, O'Cofaigh C, Palmer S, Rysgaard S, Seroussi H, Siegert MJ, Slabon P, Straneo F, van den Broeke MR, Weinrebe W, Wood M and Zinglersen KB (2017) BedMachine v3: Complete Bed Topography and Ocean Bathymetry Mapping of Greenland From Multibeam Echo Sounding Combined With Mass Conservation. *Geophysical Research Letters*, **44**(21), 11,051–11,061 (doi: 10.1002/2017GL074954)

Morlighem M, Rignot E, Binder T, Blankenship D, Drews R, Eagles G, Eisen O, Ferraccioli F, Forsberg R, Fretwell P, Goel V, Greenbaum JS, Gudmundsson H, Guo J, Helm V, Hofstede C, Howat I, Humbert A, Jokat W, Karlsson NB, Lee WS, Matsuoka K, Millan R, Mouginot J, Paden J, Pattyn F, Roberts J, Rosier S, Ruppel A, Seroussi H, Smith EC, Steinhage D, Sun B, Broeke MRvd, Ommen TDv, Wessem Mv and Young DA (2020) Deep glacial troughs and stabilizing ridges unveiled beneath the margins of the Antarctic ice sheet. *Nature Geoscience*, **13**(2), 132–137 (doi: 10.1038/s41561-019-0510-8)

Müller S, Schüler L, Zech A and Heße F (2022) `GSTools` v1.3: a toolbox for geostatistical modelling in python. *Geoscientific Model Development*, **15**(7), 3161–3182 (doi: 10.5194/gmd-15-3161-2022)

Nilsson J, Gardner A and Paolo FS (2023) MEaSUREs ITS_LIVE Antarctic Grounded Ice Sheet Elevation Change, Version 1 (doi: 10.5067/L3LSVDZS15ZV)

Nowak M and Verly G (2005) The practice of sequential gaussian simulation. In O Leuangthong and CV Deutsch (eds.), *Geostatistics Banff 2004*, 387–398, Springer Netherlands, Dordrecht, ISBN 978-1-4020-3610-1 (doi: 10.1007/978-1-4020-3610-1_39)

Ockenden H, Bingham RG, Curtis A and Goldberg D (2023) Ice-flow perturbation analysis: a method to estimate ice-sheet bed topography and conditions from surface datasets. *Journal of Glaciology*, **69**(278), 1677–1686 (doi: 10.1017/jog.2023.50)

Perego M, Price S and Stadler G (2014) Optimal initial conditions for coupling ice sheet models to earth system models. *Journal of Geophysical Research: Earth Surface*, **119**(9), 1894–1917 (doi: https://doi.org/10.1002/2014JF003181)

Pollard D and DeConto RM (2012) A simple inverse method for the distribution of basal sliding coefficients under ice sheets, applied to antarctica. *The Cryosphere*, **6**(5), 953–971 (doi: 10.5194/tc-6-953-2012)

Pralong MR and Gudmundsson GH (2011) Bayesian estimation of basal conditions on rutford ice stream, west antarctica, from surface data. *Journal of Glaciology*, **57**(202), 315–324 (doi: 10.3189/002214311796406004)

Rathmann NM and Lilien DA (2022) Inferred basal friction and mass flux affected by crystal-orientation fabrics. *Journal of Glaciology*, **68**(268), 236–252 (doi: 10.1017/jog.2021.88)

Reuschen S, Xu T and Nowak W (2020) Bayesian inversion of hierarchical geostatistical models using a parallel-tempering sequential Gibbs MCMC. *Advances in Water Resources*, **141**, 103614 (doi: 10.1016/j.advwatres.2020.103614)

Reuschen S, Jobst F and Nowak W (2021) Efficient discretization-independent bayesian inversion of high-dimensional multi-gaussian priors using a hybrid mcmc. *Water Resources Research*, **57**(8), e2021WR030051 (doi: https://doi.org/10.1029/2021WR030051)

Rignot E, Mouginot J and Scheuchl B (2017) Measures insar-based antarctica ice velocity map, version 2 (doi: 10.5067/D7GK8F5J8M8R)

Rignot E, Mouginot J, Scheuchl B, van den Broeke M, van Wessem MJ and Morlighem M (2019) Four decades of antarctic ice sheet mass balance from 1979–2017. *Proceedings of the National Academy of Sciences*, **116**(4), 1095–1103 (doi: 10.1073/pnas.1812883116)

Robel AA, Seroussi H and Roe GH (2019) Marine ice sheet instability amplifies and skews uncertainty in projections of future sea-level rise. *Proceedings of the National Academy of Sciences*, **116**(30), 14887–14892 (doi: 10.1073/pnas.1904822116)

Roberts GO and Sahu SK (2002) Updating Schemes, Correlation Structure, Blocking and Parameterization for the Gibbs Sampler. *Journal of the Royal Statistical Society: Series B (Methodological)*, **59**(2), 291–317 (doi: 10.1111/1467-9868.00070)

Roberts JL, Blankenship DD, Greenbaum JS, Beem LH, Kempf SD, Young DA, Richter TG, Van Ommen T and Le Meur E (2023) Eagle/icecap ii - geophysical observations (surface and bed elevation, ice thickness, gravity disturbance and magnetic anomalies) (doi: 10.26179/5xcc-4836)

Schoof C (2007) Ice sheet grounding line dynamics: Steady states, stability, and hysteresis. *Journal of Geophysical Research: Earth Surface*, **112**(F3) (doi: https://doi.org/10.1029/2006JF000664)

Sergienko OV and Wingham DJ (2022) Bed topography and marine ice-sheet stability. *Journal of Glaciology*, **68**(267), 124–138 (doi: 10.1017/jog.2021.79)

Seroussi H, Morlighem M, Rignot E, Larour E, Aubry D, Ben Dhia H and Kristensen SS (2011) Ice flux divergence anomalies on 79north Glacier, Greenland. *Geophysical Research Letters*, **38**(9), 2011GL047338 (doi: 10.1029/2011GL047338)

Seroussi H, Nowicki S, Simon E, Abe-Ouchi A, Albrecht T, Brondex J, Cornford S, Dumas C, Gillet-Chaulet F, Goelzer H, Golledge NR, Gregory JM, Greve R, Hoffman MJ, Humbert A, Huybrechts P, Kleiner T, Larour E, Leguy G, Lipscomb WH, Lowry D, Mengel M, Morlighem M, Pattyn F, Payne AJ, Pollard D, Price SF, Quiquet A, Reerink TJ, Reese R, Rodehacke CB, Schlegel NJ, Shepherd A, Sun S, Sutter J, Van Breedam J, van de Wal RSW, Winkelmann R and Zhang T (2019) initmip-antarctica: an ice sheet model initialization experiment of ismip6. *The Cryosphere*, **13**(5), 1441–1471 (doi: 10.5194/tc-13-1441-2019)

Shackleton C, Matsuoka K, Moholdt G, Van Liefferinge B and Paden J (2023) Stochastic simulations of bed topography constrain geothermal heat flow and subglacial drainage near dome fuji, east antarctica. *Journal of Geophysical Research: Earth Surface*, **128**(11), e2023JF007269 (doi: https://doi.org/10.1029/2023JF007269)

Siegert MJ, Ross N and Le Brocq AM (2016) Recent advances in understanding antarctic subglacial lakes and hydrology. *Philosophical Transactions of the Royal Society A: Mathematical, Physical and Engineering Sciences*, **374**(2059), 20140306 (doi: 10.1098/rsta.2014.0306)

Sun S, Cornford SL, Liu Y and Moore JC (2014) Dynamic response of antarctic ice shelves to bedrock uncertainty. *The Cryosphere*, **8**(4), 1561–1576 (doi: 10.5194/tc-8-1561-2014)

Teisberg TO, Schroeder DM and MacKie EJ (2021) A Machine Learning Approach to Mass-Conserving Ice Thickness Interpolation. In *2021 IEEE International Geoscience and Remote Sensing Symposium IGARSS*, 8664–8667 (doi: 10.1109/IGARSS47720.2021.9555002)

van Pelt WJJ, Oerlemans J, Reijmer CH, Pettersson R, Pohjola VA, Isaksson E and Divine D (2013) An iterative inverse method to estimate basal topography and initialize ice flow models. *The Cryosphere*, **7**(3), 987–1006 (doi: 10.5194/tc-7-987-2013)

van Wessem JM, van de Berg WJ, Noël BPY, van Meijgaard E, Amory C, Birnbaum G, Jakobs CL, Krüger K, Lenaerts JTM, Lhermitte S, Ligtenberg SRM, Medley B, Reijmer CH, van Tricht K, Trusel LD, van Ulft LH, Wouters B, Wuite J and van den Broeke MR (2018) Modelling the climate and surface mass balance of polar ice sheets using racmo2 – part 2: Antarctica (1979–2016). *The Cryosphere*, **12**(4), 1479–1498 (doi: 10.5194/tc-12-1479-2018)

Weertman J (1974) Stability of the junction of an ice sheet and an ice shelf. *Journal of Glaciology*, **13**(67), 3–11 (doi: 10.3189/S0022143000023327)

Werder MA, Huss M, Paul F, Dehecq A and Farinotti D (2020) A bayesian ice thickness estimation model for large-scale applications. *Journal of Glaciology*, **66**(255), 137–152 (doi: 10.1017/jog.2019.93)

Wernecke A, Edwards TL, Holden PB, Edwards NR and Cornford SL (2022) Quantifying the Impact of Bedrock Topography Uncertainty in Pine Island Glacier Projections for This Century. *Geophysical Research Letters*, **49**(6), e2021GL096589 (doi: 10.1029/2021GL096589)

Young DA, Wright AP, Roberts JL, Warner RC, Young NW, Greenbaum JS, Schroeder DM, Holt JW, Sugden DE, Blankenship DD, van Ommen TD and Siegert MJ (2011) A dynamic early east antarctic ice sheet suggested by ice-covered fjord landscapes. *Nature*, **474**(7349), 72–75 (doi: 10.1038/nature10114)

Young DA, Schroeder DM, Blankenship DD, Kempf SD and Quartini E (2016) The distribution of basal water between antarctic subglacial lakes from radar sounding. *Philosophical Transactions of the Royal Society A: Mathematical, Physical and Engineering Sciences*, **374**(2059), 20140297 (doi: 10.1098/rsta.2014.0297)

Zuo C, Yin Z, Pan Z, MacKie EJ and Caers J (2020) A Tree-Based Direct Sampling Method for Stochastic Surface and Subsurface Hydrological Modeling. *Water Resources Research*, **56**(2), e2019WR026130 (doi: 10.1029/2019WR026130)

A Markov chain Monte Carlo approach for geostatistically simulating mass conserving subglacial topography (Supplementary Materials)

Niya Shao[1], Emma Mackie[1], Michael Field[1], and Felicity McCormack[2]

[1]Department of Geological Sciences, University of Florida, Gainesville, FL, USA.
[2]Securing Antarctica's Environmental Future, School of Earth, Atmosphere and Environment, Monash University, Clayton, Kulin Nations, Victoria, Australia.

1 Equality of Proposal Distribution

The update methods used in the MCMC algorithm satisfy the equation $q(x, y) = q(y, x)$ for any x and any y, where $q(x, y)$ denotes the probability of obtaining x by updating y once. In this section, we provide further explanation for how the equation is satisfied in the three different MCMC chains. In the preprocessing chain's update method, the random fields used for perturbing topography are sampled from a multivariate Gaussian distribution with zero mean. The random field used to obtain y from x is exactly the random field used to obtain x from y with an opposite sign, which has the same probability of being generated. Similarly, Weighted Random Fields (WRFs) used in the meso-scale chains are generated by multiplying weight matrices with random fields. The WRF used to obtain y from x has the same probability of being generated as the WRF used to obtain x from y. Thus, $q(x, y) = q(y, x)$ for any x and any y in both preprocessing and meso-scale chains. Fine-scale chains utilize blocks of SGS to update the topography. y is generated from x by selecting a block, deleting grid cells inside the block that are not radar-measured bed elevations, and re-simulating deleted grid cells. To generate x from y, the same block needs to be selected. Knowing that SGS generates independent topography realizations that are equiprobable, the probability of generating y is the same as the probability of generating x. Thus, $q(x, y) = q(y, x)$ for any x and y in the fine-scale chains. The only exception to this equation happens when transiting between meso-scale and fine-scale chains. Because the topographies sampled at the end of the meso-scale chains may not satisfy SGS properties, the assumption of equiprobable realizations within the update block is not satisfied. Since this transition only happens once for every grid cell, the effect is estimated to be not significant.

2 Weighted Random Field Calculations

In the meso-scale chains, weighted random fields iteratively update the topography while preserving the conditioning bed elevations. We generate the weighted random fields by multiplying a random field with the data weight matrix and the edge weight matrix. The data weights matrix $w(d_c, d_{cmax})$ helps to avoid perturbations at grid cells with conditioning data. $w(d_c, d_{cmax})$ is calculated from the distance of every grid cell to their closest conditioning data d_c with a logistic function (equation s1), such that the weights are 0 at locations of conditioning data and gradually change to 1 at location at least d_{cmax} away from any conditioning data. d_{cmax} represents the separation distance between two grid cells at which the correlation of their bed elevations vanishes. d_{cmax} is set to the range of the spherical variogram fitted to the conditioning bed elevation data, which is 46 km in the studying region. In addition, the edge weights matrix $w(d_e, d_{emax})$ assists in avoiding sudden change at the edge of the random field block when adding the block to topography. $w(d_e, d_{emax})$ is calculated using the same logistic function (equation s1) but calculated for the distances to edges of the update block, d_e. The weight gradually changes from 0 at the edges to 1 at locations that are at least d_{emax} away from the edges. Similarly, d_{emax} is determined from the range of the spherical variogram (46 km) in the studying area. Multiplying the data weight matrix and the edge weight matrix with the random field ensures that the resulting weighted random field changes smoothly from 0 at conditioning data locations and blocks edges to the random field's values elsewhere.

$$\begin{aligned} d_n(d, d_{max}) &= \begin{cases} 1, & \text{if } d \geq d_{max} \\ \frac{d}{d_{max}}, & \text{otherwise} \end{cases} \\ w(d, d_{max}) &= \left(\frac{2}{1+\exp(-6d_n)}\right) - 1 \end{aligned} \tag{s1}$$

3 Preprocessing Chain Results

Fig. S1 includes additional details about the results of the preprocessing chain. In Fig. S1(a), we find that the end topography of the preprocessing chain reconstructs a shallower trench while deviating from some grid cells containing radar-measured bed elevations. This could be caused by a mismatch between the Gaussian distribution used to model the bed elevation errors and the presence of certain conditioning grid cells with large errors, possibly caused by radar clutters.

We calculate the standard deviation of the difference between the topography sampled from the preprocessing chain and the radar-measured bed elevations. Grid cells with elevation measurements exceeding the generated topography by more than 1.5 standard deviations are identified. Additionally, we manually select 10 grid cells in the vicinity of the Denman trough, which could potentially be corrupted by clutter. In total, 138 grid cells – highlighted in red in Fig. S1(b) – are excluded from the conditioning data used in the meso-scale and fine-scale chains.

4 Autocorrelation

Fig. S2(b) showcases the autocorrelation of individual grid cells in one of the meso-scale chain from iteration 200,000 to iteration 210,000. Fig. S2(a) plots the location of grid cells randomly chosen to generate Fig. S2(b). We observe that the autocorrelation converge to 0 before the 4000 iterations lag with a slight tendency toward negative autocorrelation values.

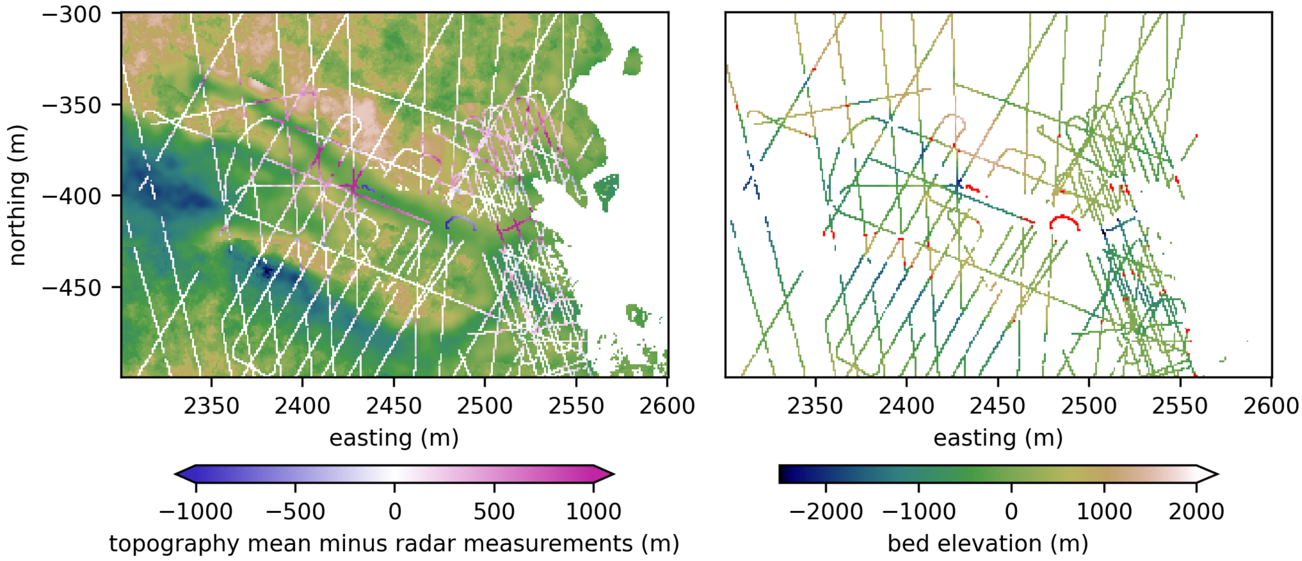

Figure S1: Subplot (a) shows the elevation differences between topography from the preprocessing chain and the radar-measured topography, which is overlaid upon the end topography sample generated in the preprocessing chain. Subplot (b) shows the radar-measured topography and the excluded bed elevation measurements highlighted in red

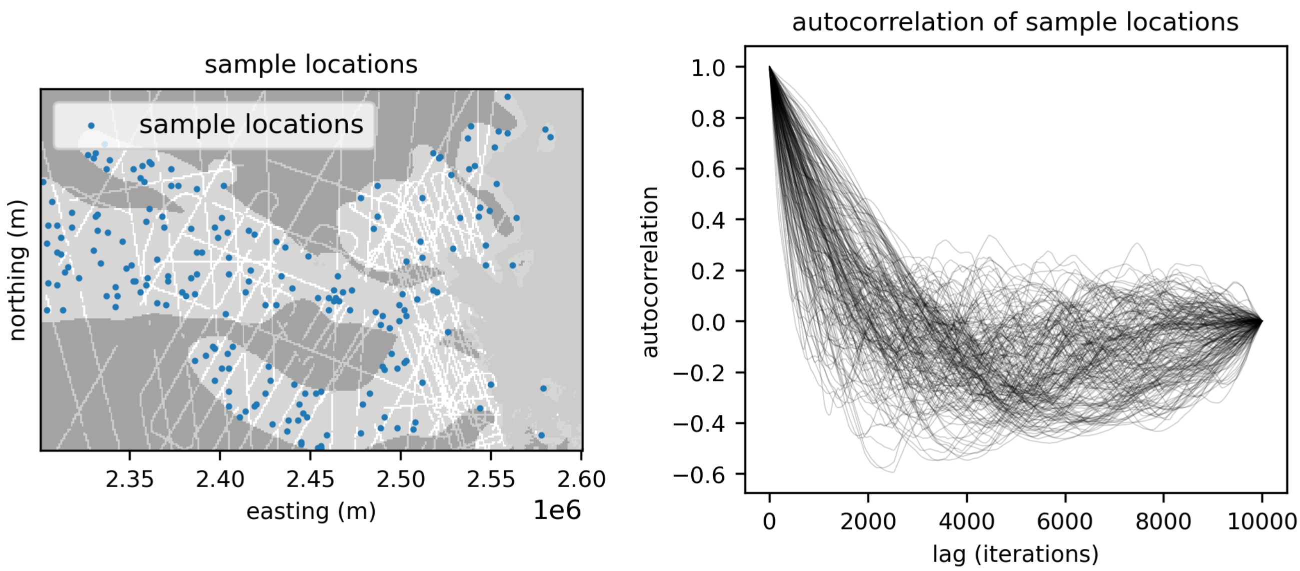

Figure S2: Subplot (a) shows the high velocity region (light grey), the location of conditioning bed measurements (semi-transparent white), and the grid cells used to generate subplot (b). Subplot (b) plots the autocorrelation of 200 grid cells in one of the meso-scale chains from iteration 200,000 to iteration 210,000.